UNIVERSITÀ DEGLI STUDI DI PADOVA

DIPARTIMENTO DI BIOLOGIA

Corso di Laurea in Biologia Molecolare

ELABORATO DI LAUREA

Analisi molecolare delle cause dell'anosmia, correlata all'infezione da SARS-CoV-2, nell'epitelio olfattivo e cervello dell'uomo e dei criceti

Tutor: Prof. Cristiano De Pitta'
Dipartimento di Biologia

Co-tutor: Dott. Lorenzo Lupi
Dipartimento di Medicina molecolare

Laureanda: Sara Scarpa

ANNO ACCADEMICO 2022/2023

INDICE

ABSTRACT

Fin dall'insorgenza della pandemia, la perdita di gusto e olfatto sono risultati sintomi dell'infezione da *SARS-CoV-2*. Per identificare i meccanismi molecolari alla base di questi sintomi, sono stati infettati con *SARS-CoV-2* individui di criceto siriano, animale modello per riprodurre il decorso della malattia da COVID-19. Sono stati analizzati campioni di mucosa olfattiva proveniente da pazienti umani e animali, con lo scopo di individuare la tipologia di cellule infettate da *SARS-CoV-2* ed eventuali variazioni a livello di epitelio olfattivo. I risultati delle analisi hanno mostrato una disorganizzazione a livello di alcune aree di epitelio olfattivo, che presentano cellule deciliate o in apoptosi. È stato, inoltre, rilevato un alto numero di neuroni sensoriali olfattivi in fase di fagocitosi da parte di cellule del sistema immunitario. Questo risultato suggerisce che la possibile causa dell'anosmia sia la morte dei neuroni sensoriali olfattivi. Infine, è stato studiato il possibile meccanismo che *SARS-CoV-2* può impiegare per raggiungere il sistema nervoso centrale, mostrando come l'infezione possa avvenire per via retrograda, a partire dal sistema olfattivo, oltre a presentare una risposta immunitaria a livello di epitelio olfattivo

1. Introduzione

1.1 Syrian hamster come organismo modello per SARS-CoV-2

Il criceto siriano (*Mesocricetus auratus*) è un piccolo mammifero utilizzato come organismo modello per lo studio di infezioni da parte di virus respiratori come *Severe Acute Respiratory Syndrome Coronavirus 1* (*SARS-CoV-1*), *influenzavirus*, *adenovirus* e per *Severe Acute Respiratory Syndrome Coronavirus 2* (*SARS-CoV-2*). È diventato un modello molto utilizzato per questa patologia, in quanto ricapitola molte caratteristiche tipiche di pazienti con un decorso moderato della malattia, come la correlazione tra l'età e la gravità del decorso della malattia (Gruber *et al*., 2022). Il criceto è un roditore dalla struttura corpulenta, l'adulto può raggiungere un peso tra i 120 e i 150 g e possiede un'aspettativa di vita di circa 1-2 anni, con gli esemplari maschi caratterizzati da un'aspettativa di vita maggiore e dimensioni inferiori rispetto alle femmine (Hubrecht & Kirkwood, 2010). Quando l'enzima ACE2 umano (*Angiotensin-converting enzyme 2, ACE2*), che interagisce con il dominio di legame RBD (*receptor-binding domain, RBD*) di *SARS-CoV-2*, è stato scoperto essere il principale recettore cellulare per la proteina virale Spike (S), analisi strutturali di ACE2 in mammiferi hanno dimostrato che ACE2 dei criceti presenta un'alta omologia con quello umano rendendoli suscettibili all'infezione da *SARS-CoV-2* (Gruber *et al*., 2022). I criceti infettati presentano disturbi respiratori, letargia, una postura incurvata, pelo arruffato e perdite di peso, recuperando generalmente dalla malattia in due settimane. Alcuni tra gli animali infettati presentavano segni di anosmia e/o ageusia (Muñoz-Fontela *et al*., 2020) tra i 2 e i 5 giorni dall'infezione (*dpi, days post-inoculation*). Il criceto, dunque, si rivela essere un buon organismo modello per lo studio della patogenesi da *SARS-CoV-2*, in quanto la patologia sviluppata in seguito all'infezione risulta essere molto simile a quella sviluppata in uomo.

1.2 SARS-CoV-2

SARS-CoV-2, il virus responsabile del COVID-19, è emerso per la prima volta a Wuhan in Cina, nel dicembre 2019, con i primi casi emersi in un mercato ittico (Ochani *et al*., 2021). Diversi pazienti con polmonite di eziologia sconosciuta vengono segnalati in vari ospedali a Wuhan, portando all'identificazione dell'agente patogeno l'8 gennaio 2020 e alla dichiarazione di pandemia l'11 marzo 2020 (Ochani *et al*., 2021). *SARS-CoV-2* appartiene al genere virale beta-CoV, categoria che comprende anche *SARS-CoV-1*, e *Middle Eastern Respiratory Syndrome CoV* (*MERS-CoV*). I Coronavirus sono suddivisi in 4 gruppi basati sulla sierologia: alpha, beta, gamma e delta; tra questi, i virus alpha e beta infettano i mammiferi, i gamma le specie aviarie, mentre i delta possono infettare sia i mammiferi sia le specie aviarie (Ochani *et al*., 2021). La trasmissione di *SARS-CoV-2* tipicamente avviene tramite goccioline provenienti dalla respirazione, il periodo di incubazione medio è di 6.4 giorni (Ochani *et al*., 2021). La maggioranza dei pazienti tende ad avere un decorso lieve della malattia, ma una minoranza sviluppa una grave ipossia (carenza di ossigeno a livello tissutale), la quale richiede ospedalizzazione e ventilazione meccanica (Ochani *et al*., 2021). Anche *SARS-CoV-2*, come *SARS-CoV-1*, utilizza ACE2 come recettore *target*, altamente espresso sulla superficie luminale delle cellule epiteliali alveolari di tipo II (Ochani *et al*., 2021). La fase clinica di *SARS-CoV-2* può essere suddivisa in tre

fasi: “fase di viremia”, in cui il virus entra nel sangue periferico dai polmoni, “fase acuta della malattia”, in cui gli individui diventano fortemente critici, e “fase di recupero” (Ochani *et al*., 2021). Nel dicembre 2019, i sintomi riportati erano mancanza di respiro, tosse, febbre e diarrea, e una gravità della malattia che varia da lieve a grave, anche se molti dei pazienti che contraggono il virus rimangono asintomatici, seppur contagiosi (Ochani *et al*., 2021). Le persone di età più anziana (dai 65 anni in poi) sono caratterizzate da un più alto rischio di sviluppare una forma severa, anche se gli adulti più giovani possono ugualmente necessitare di un ricovero in ospedale, seppur con una frequenza più bassa (Ochani *et al*., 2021). Tra i vari sintomi riportati dai pazienti affetti da COVID-19, vi è una perdita improvvisa dell’olfatto (anosmia) e del gusto (ageusia) durante le prime fasi del decorso della malattia, rilevata in circa il 45% dei pazienti (Koyama *et al*., 2021). Il meccanismo provocato da *SARS-CoV-2* alla base della disfunzione olfattiva non è ancora ben caratterizzato (Koyama *et al*., 2021).

1.3 L’epitelio olfattivo e le sue componenti

L’epitelio olfattivo (*Olfactory Epithelium, OE*) è una struttura pseudo-stratificata che riveste la parte superiore/dorsale della cavità nasale (Liang, 2020). Oltre ai neuroni sensoriali olfattivi (*Olfactory Sensory Neurons, OSN*), l’OE comprende anche le cellule sustentacolari (*Olfactory Sustentacular Cells, OSC*), le cellule basali e le cellule del dotto delle ghiandole di Bowman (Fig. 1) (Liang, 2020). I OSN sono responsabili della ricezione olfattiva e della trasduzione, le loro proiezioni assoniche nel bulbo olfattivo permettono il trasferimento dei segnali olfattivi al sistema nervoso centrale (Liang, 2020), e sono esposte direttamente, tramite l’estremità dendritica, al muco nasale e a potenziali agenti dannosi o microorganismi presenti nell’aria nella cavità nasale (Liang, 2020). In base all’espressione dei recettori olfattivi accoppiati alla proteina G (GPCR), i OSN nell’OE si differenziano in vari sottogruppi, ognuno dei quali presenta un solo tipo di recettori (Liang, 2020). Gli assoni provenienti da uno stesso sottogruppo di OSN convergono per poi proiettare verso un singolo, o alcuni glomeruli del bulbo olfattivo (Liang, 2020). Le OSC, si ritengono possedere sia funzioni epiteliali che gliali, funzionando come supporto fisico, metabolico, secretorio e di assorbimento per i OSN (Liang, 2020). Queste cellule sono in grado di avvolgere il corpo, i dendriti e gli assoni dei OSN in maniera parziale o totale in funzione dello stato di maturazione del neurone, mentre le cellule basali rappresentano il precursore delle cellule staminali dell’epitelio (Liang, 2020). L’OE svolge funzioni sia epiteliali che sensoriali, in quanto protegge e separa strutture più profonde dall’aria che entra a contatto con la cavità nasale, ed è il sito in cui avvengono la percezione olfattiva e la trasduzione dei segnali (Liang, 2020).

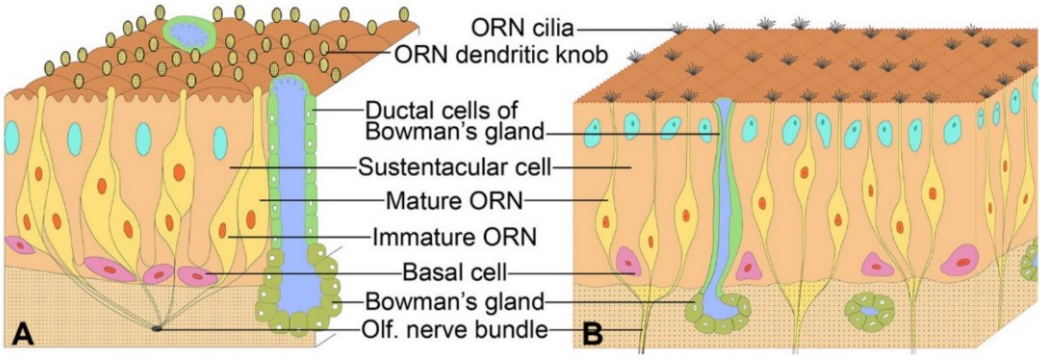

Figura 1. Rappresentazione schematica dell’organizzazione dell’epitelio olfattivo (tratto da Liang, 2020).

2. Materiali e metodi

2.1 Descrizione del disegno sperimentale

Campioni di mucosa olfattiva umana sono stati prelevati da 16 individui (12 pazienti con COVID-19 e 4 controlli sani) all'ENT (*Ear, Nose and Throat*) Department del Lariboisière Hospital a Parigi, in Francia, tra maggio e ottobre 2020. Tutti gli animali, arruolati in questo studio, sono stati inseriti casualmente nei differenti gruppi sperimentali. Per l'analisi della mucosa umana, sono stati raccolti due campioni nasali da ciascun partecipante (un campione per narice, uno immediatamente congelato e l'altro fissato in formalina), ed ognuno è stato analizzato tre volte tramite test per la rilevazione di *SARS-CoV-2* tramite PCR (campioni congelati) e immunoistochimica (campioni in formalina). Campioni nasali di due pazienti e due controlli sono anche stati titolati per *SARS-CoV-2* in colture cellulari. Negli esperimenti animali, almeno quattro maschi sono stati utilizzati per ogni *time point* (corrispondenti a 2, 4 e 14 dpi), e la replica è stata eseguita con lo stesso numero di femmine. I procedimenti di rilevazione del virus e di titolazione sono stati effettuati seguendo il medesimo protocollo sia per campioni umani che animali. Campioni di mucosa olfattiva di due controlli e cinque criceti infetti sono stati analizzati per la rilevazione di *SARS-CoV-2* tramite Microscopio Elettronico a Scansione (*SEM*), e due controlli e tre criceti infetti tramite immunofluorescenza. Per la quantificazione al microscopio, il titolo virale di ciascun animale è stato calcolato come la media di quattro-otto campi quantificati indipendentemente l'uno dall'altro.

2.2 Caratteristiche dei soggetti arruolati nello studio

I soggetti che presentavano una perdita delle funzioni olfattive e che si erano rivolti al Lariboisière Hospital per una sospetta o confermata infezione da *SARS-CoV-2* sono stati inclusi nello studio. La patologia acuta per questi pazienti è sempre stata sintomatica e dimostrata da analisi cliniche [almeno un test *SARS-CoV-2* RT-PCR risultato positivo o in alternativa un test sierologico *SARS-CoV-2*], o probabile se rispettava almeno uno dei criteri principali: anosmia/ageusia, contatto con un caso positivo a PCR, polmonite bilaterale, o tre criteri minori, tra cui febbre, mal di testa, fatica, mialgie, tosse, dolore e/o sensibilità al petto, tachicardia inspiegabile, diarrea e geloni. Sono stati reclutati in questo studio anche pazienti di controllo che si erano recati all'ENT Department, ma che non presentavano test biologici positivi a COVID-19 o sospetto COVID-19 nelle precedenti 8 settimane, e nessun sintomo che potesse suggerire un'infezione da *SARS-CoV-2* o qualsiasi altra malattia respiratoria, e dunque nessuna perdita di funzioni olfattive o gustative. Tutti i pazienti sono stati sottoposti ad anamnesi e visita ORL eseguita da un medico certificato ENT. Sono stati eseguiti i seguenti test: valutazione delle funzioni olfattive e gustative attraverso un questionario e l'utilizzo di una Scala Analogica Visiva (*VAS*) che va da 0 mm a 100, attraverso cui i partecipanti hanno eseguito un'autovalutazione della loro percezione di gusto e olfatto, e tamponi nasali per la raccolta di cellule neuroepiteliali e della mucosa olfattiva. La VAS consiste in un metodo non invasivo e preciso per le misurazioni in ambito sanitario. Il paziente è invitato a tracciare una X all'interno di una linea in cui l'estremità destra indica l'inabilità totale di odorare e gustare (0 mm), mentre l'altra rappresenta una normale percezione di gusto e olfatto (100 mm).

Successivamente viene determinato il punteggio, misurando la distanza in mm tra il punto d'inizio e il segno del paziente. Si possono quindi unire le risposte fornite dai pazienti all'interno di una scala fissa, facilitando così il campionamento e di conseguenza l'interpretazione dei risultati.

2.3 Tamponi nasali per la raccolta di mucosa olfattiva

Un medico ha prelevato campioni di mucosa olfattiva, da ciascun soggetto, tramite tamponi nasali nel rispetto delle misure di sicurezza e dopo l'applicazione locale di Xylocaina (lidocaina, 5%). Il campionamento è stato eseguito con un tampone endocervicale da 3,5 mm (Gyneas, Goussainville, France) inserito e delicatamente ruotato per cinque volte all'interno di entrambe le narici (360°). I tamponi (uno per narice) sono stati poi posti in ghiaccio immediatamente dopo il campionamento e congelati a -80°C, o immersi in una soluzione di formalina neutralizzata al 10% (anche definita formaldeide 4%) (Sigma-Aldrich).

2.4 Produzione e titolazione del virus SARS-CoV-2

Il ceppo 2019-nCoV/IDF0372/2020 è stato fornito dalla Professoressa Sylvie Van der Werf dell'Institut Pasteur a Parigi. Le scorte virali sono state prodotte in cellule Vero-E6 infettate con un titolo di infezione pari a $1x10^{-4}$ PFU (*Plaque-Forming Unit*). Il virus è stato raccolto 3 giorni dopo l'infezione, purificato e poi aliquotato prima di essere conservato a 80°C. Stock virali sono stati titolati in cellule Vero-E6 tramite saggio delle placche utilizzando strati semisolidi (Avicel, DuPont).

2.5 Modello di SARS-CoV-2 in criceto

Criceti siriani maschi e femmine, di età compresa tra le 5 e le 6 settimane (peso medio tra i 60 e gli 80 g), sono stati acquistati dai laboratori Janvier Labs e stabulati in ambienti privi di patogeni. I criceti sono stati mantenuti a gruppi di 4 individui in gabbie all'interno di un impianto di biosicurezza di livello 3, con accesso illimitato ad acqua e cibo. Prima di ogni manipolazione, gli animali sono stati sottoposti ad un periodo di acclimatazione di 1 settimana. Gli animali sono stati anestetizzati tramite iniezione intraperitoneale di Ketamina (200 mg/kg; Imalgène 1000 Merial) e Xilazina (10 mg/kg; Rompun, Bayer), e poi 100 µl di soluzione fisiologica contenente $6x10^4$ PFU di *SARS-CoV-2* sono stati somministrati per via nasale a ciascun animale (50 µl per narice), mentre i controlli hanno ricevuto solo la fisiologica. Animali infetti e non sono stati alloggiati in gabbie separate, e tutti i criceti sono stati monitorati giornalmente, per il peso corporeo e punteggio clinico, quest'ultimo basato su una scala cumulativa che va da 0 a 4 che si basa sulla presenza di pelo arruffato, movimenti rallentati, apatia e stress quando manipolati. In momenti predefiniti post infezione, gli animali sono stati sottoposti a test comportamentali o sottoposti a eutanasia, con conseguente raccolta di campioni di turbinati nasali, trachea, polmoni e cervello (separato in bulbi olfattivi, cervelletto, corteccia e tronco encefalico), immediatamente congelati a -80°C o fissati in formaldeide dopo perfusione transcardica con soluzione fisiologica contenente eparina ($5x10^3$ U/ml) (Choay, Sanofi), seguita da formaldeide 4%.

2.6 Test comportamentali

Tutti i test comportamentali sono stati eseguiti in gabbie all'interno di un impianto di biosicurezza di livello 3.

1. Test sulla preferenza del saccarosio:

Il gusto nei criceti è stato misurato tramite un test basato sulla scelta tra due bottiglie, una contenente semplice acqua, e una contenente saccarosio al 2%. Una riduzione della preferenza del saccarosio negli individui infetti rispetto a quelli non infetti è indicativa della presenza di anomalie per quanto riguarda il gusto. Dopo 6 ore di deprivazione dell'acqua, è stato condotto un test individuale notturno, che corrisponde al periodo di attività naturale del criceto.

2. Test di individuazione del cibo sotterrato:

I criceti sono stati utilizzati una volta sola per ogni test. Quattro giorni prima del test, i criceti hanno ricevuto cereali al cioccolato (Coco Pops, Kellog's) che hanno mangiato in 1 ora. Venti ore prima del test, i criceti sono stati messi a digiuno e poi posti individualmente all'interno di una nuova gabbia (37 cm x 29 cm x 18 cm) con un ambiente sterile per 20 minuti. Sono poi stati posti per due minuti in un'altra gabbia simile, in cui sono stati nascosti tra i 10 e i 12 pezzi di cereali ad 1,5 cm di profondità, nell'angolo opposto rispetto a quello in cui sono stati posizionati i criceti. È stata quindi registrata attraverso un cronometro la latenza per trovare il cibo (definita come il tempo per localizzare i cereali ed iniziare a scavare). Il test è stato effettuato per una durata di 15 minuti. Appena il cibo è stato scoperto, i criceti sono stati poi rimossi dalla gabbia. Un minuto dopo, i criceti hanno effettuato lo stesso test, ma con cereali al cioccolato ben visibili, posizionati al di sopra del suolo.

2.7 Microscopia elettronica a scansione (SEM)

Dopo perfusione transcardica con PBS (Phosphate Buffered Saline, soluzione tampone) e formaldeide 4%, le teste e i polmoni dei criceti sono state fissate per intero in formaldeide 4% (Sigma-Aldrich) a 4°C per 1 settimana, per permettere la neutralizzazione del virus. I polmoni e L'OE sono stati sezionati in modo da ottenere piccoli campioni di ciascuna porzione, e post-fissati tramite incubazione in glutaraldeide 2.5% in 0.1 M di cacodilato di sodio per 1 ora a temperatura ambiente e poi per 12 ore a 4°C. I campioni sono stati lavati in cacodilato di sodio 0.1 M e poi più volte in acqua, e processati tramite un'alternanza di incubazioni in tetrossido di osmio 1% e in tiocarboidrazide (tramite metodo OTOTO). Dopo una deidratazione tramite incubazione in concentrazioni crescenti di etanolo, i campioni sono stati essiccati, montati su vetrini, e analizzati tramite SEM a Field Emission, con un Jeol JSM6700F, operante a 3 kV.

2.8 Immunofluorescenza

Tessuti provenienti da animali perfusi con paraformaldeide (PFA) sono stati fissati in PFA 4% per 1 settimana, e tamponi olfattivi provenienti dai pazienti sono stati mantenuti in PFA fino ad ulteriore utilizzo. Successivamente, le teste intere (prive di pelle e mascella inferiore) sono state decalcificate in TBD-2 (Thermo Fisher Scientific) per 3-5 giorni, tagliate a metà lungo il piano sagittale e risciacquate in PBS. Organi e tamponi sono stati lavati in PBS e disidratati in saccarosio 30%, per essere integrati in un composto avente temperatura di taglio ottimale (O.C.T.) (Tissue-Tek), congelati in ghiaccio secco, e sezionati con criostato in sezioni spesse 20 μm per gli organi di criceto e 14 μm per i tamponi. I

campioni sezionati sono stati lavati in PBS, e il recupero dell'epitopo è stato effettuato tramite incubazione dei campioni in tampone citrato (pH 6.0; Sigma-Aldrich) per 20 min a 96°C, o durante la notte a 60°C per le sezioni di testa di criceto, inclini a staccarsi dai vetrini. Le sezioni sono state bloccate in PBS arricchito con siero di capra 10%, siero fetale di vitello 4%, e Triton X-100 0.4% per 2 ore a temperatura ambiente, seguito da un'incubazione notturna a 4°C con anticorpi primari: rat anti-CD11b (1/100; BD Biosciences), rabbit anti-SARS-CoV NP (1/500; fornito da N. Escriou, Institut Pasteur, Paris), mouse anti-OMP (1/250; Santa Cruz Biotechnology), chicken anti-Iba1 (1/500; Synaptic Systems), mouse anti-Tuj1 (1/250; Thermo Fisher Scientific), mouse anti-PGP9.5 (1/500; Abcam), e rabbit anti-cleaved caspase-3 (1/250; Cell Signaling Technology, Asp175). Dopo il risciacquo, le sezioni sono state incubate con gli anticorpi secondari appropriati (1/500; goat anti-rat Alexa Fluor 546; goat anti-rabbit Alexa Fluor 488; goat anti-mouse IgG2a Alexa Fluor 546; goat anti-chicken Alexa Fluor 647; Invitrogen) per 2 ore a temperatura ambiente. Tutte le sezioni sono state sottoposte a controcolorazione con Hoechst (Invitrogen) prima di essere osservate con un microscopio confocale invertito Zeiss LM 710. La quantificazione delle cellule è stata fatta utilizzando il software ImageJ in modalità semi-automatica.

2.9 Isolamento dell'RNA totale e analisi di espressione genica in campioni umani

Campioni di tamponi congelati sono stati incubati in TRIzol (Invitrogen) per 5 minuti, e l'RNA totale è stato estratto utilizzando il Kit Direct-zol RNA MicroPrep (Zymo Research). La presenza di *SARS-CoV-2* nei campioni è stata valutata tramite one-step qRT-PCR in una piastra da PCR da 96 pozzetti, tramite l'utilizzo di un termociclatore (7500 Real-Time PCR System, Applied Biosystems). 5 µl di RNA diluito (1:10) sono stati aggiunti a 20 µl della mix SuperScript III Platinum One-Step qRT-PCR mix (Invitrogen) seguendo il protocollo, utilizzando i primer nCoV_IP2, aventi come *target* il gene *RdRp* (nCoV_IP2-12669 *forward*: 5′-ATGAGCTTAGTCCTGTTG-3′; nCoV_IP2-12759 *reverse*: 5′-CTCCCTTTGTTGTGTTGT-3), La quantificazione del carico virale in questi campioni è stata eseguita tramite una TaqMan one-step qRT-PCR (Invitrogen), con gli stessi primer nCoV_IP2 e la stessa sonda nCoV_IP2 (5′-FAM-AGATGTCTTGTGCTGCCGGTA- 3′-TAMRA), per una concentrazione finale 1 µM. La rilevazione dell'RNA virale genomico e sub-genomico è stata basata sul gene E, attraverso una TaqMan one-step qRT-PCR: per rilevare l'RNA genomico, sono stati utilizzati sonde e primer E_Sarbeco (E_Sarbeco_F1 5′-ACAGGTACGTTAATAGTTAATAGC-GT-3′; E_Sarbeco_R2 5′-ATATTGCAGCAGTACGCACACA-3′; E_Sarbeco_Probe FAM-5′-ACACTAGCCATCCTTACTGC-GCTTCG-3′-TAMRA). La rilevazione dell'RNA sub-genomico di *SARS-CoV-2* è stata ottenuta tramite sostituzione del primer E_Sarbeco_F1 con il primer CoV2sgLead (CoV2sgLead forward: 5′-CGATCTCTTG-TAGATCTGTTCTC-3′). Un gene sintetico codificante il target per la PCR è stato ordinato dall'azienda Thermo Fisher Scientific, amplificato tramite una polimerasi Phusion High-Fidelty DNA Polymerase (Thermo Fisher Scientific), e poi trascritto in vitro con il kit RiboMAX T7 (Promega). L'RNA è stato quantificato attraverso il kit Qubit RNA HS Assay (Thermo Fisher Scientific), normalizzato, e utilizzato come controllo positivo per quantificare il numero assoluto di copie di RNA. L'RNA totale proveniente dai tamponi umani è

stato anche retrotrascritto utilizzando il kit SuperScript IV VILO Master Mix (Invitrogen). Per quantificare la trascrizione dei mediatori dell'infiammazione è stata effettuata una qPCR in un volume finale di 10 µl per reazione in piastre da PCR da 384 pozzetti utilizzando un termociclatore (QuantStudio 6 Flex, Applied Biosystems). 2.5 µl di cDNA (12.5 ng) sono stati aggiunti a 7.5 µl di una master mix contenente 5 µl di Power SYBR green mix (Applied Biosystems) e 2.5 µl di acqua nucleasi-free contenente primer pre-disegnati (no. 249900, Qiagen; QuantiTect Primer Assays IL-6: QT00083720; CXCL10: QT01003065; CCL5: QT00090083; Mx1: QT00090895; ISG20: QT00225372; OMP: QT00237055; and GAPDH: QT00079247) seguendo il protocollo fornito.
Le variazioni nell'espressione genica sono state calcolate come l'n-fold del cambio di espressione nei tessuti, confrontati con i tessuti del controllo #1.

2.10 Isolamento dell'RNA totale e analisi di espressione genica in tessuti di Syrian hamster

I tessuti congelati sono stati omogeneizzati in TRIzol (Invitrogen). È stato poi raccolto il surnatante, da cui l'RNA totale è stato estratto utilizzando il kit Direct-zol RNA MicroPrep Kit (Zymo Research; per bulbo olfattivo, trachea e turbinati nasali) o un kit MiniPrep (Zymo Research; per polmoni, tronco encefalico, corteccia cerebrale e cervelletto), e retrotrascritto utilizzando la mix SuperScript IV VILO Master Mix (Invitrogen). È stata effettuata una qPCR in un volume finale di 10 µl per reazione in una piastra per PCR da 384 pozzetti, utilizzando un termociclatore (QuantStudio 6 Flex, Applied Biosystems) e 2.5 µl di acqua nucleasi-free contenente i primer nCoV_IP2 in una concentrazione finale 1 µM. Le condizioni di amplificazione sono state le stesse utilizzate per la quantificazione dei marcatori dell'infiammazione precedentemente descritti. La quantificazione del carico virale nel tessuto dei criceti è stata valutata attraverso regressione lineare utilizzando una curva standard di otto quantità conosciute di plasmidi contenenti la sequenza RdPd (che spaziano da 10^7 a 10^0 copie). La soglia di rilevazione è stata stabilita a 200 copie virali/µg di RNA. I geni *target* del criceto sono stati selezionati per quantificare i trascritti dei marcatori dell'infiammazione, utilizzando i geni *Hprt* (ipoxantina-guanina fosforibosiltransferasi) e quello della *ϒ-actina* come riferimento. Le variazioni nell'espressione genica sono state calcolate come old change nei tessuti dei criceti infetti, confrontati con i tessuti degli individui non infetti tramite il metodo $2^{-\Delta\Delta Ct}$.

2.11 Titolazione dei tamponi nasali umani e dei cervelli di criceto siriano

Campioni di tamponi congelati dei pazienti #14 e #15 e dei controlli #3 e #4 sono stati incubati con 1 ml di terreno DMEM, integrato con 1% di penicillina/streptomicina in provette da 2 ml Lysing Matrix M (MP Biomedicals) usando il seguente schema: omogeneizzazione a 4.0 m/s per 20 s, incubazione a 4°C per 2 min e una nuova omogeneizzazione a 4.0 m/s per 20 s. Le provette sono state centrifugate a 10,000xg per 1 min a 4°C. I surnatanti sono stati titolati in cellule Vero-E6 attraverso il classico saggio di placca utilizzando strati semisolidi. L'RNA è stato isolato dal surnatante utilizzando TRIzol LS (Invitrogen) e il kit Direct-zol RNA MicroPrep Kit (Zymo Research), come descritto in precedenza.

2.12 Analisi trascrittomica nel bulbo olfattivo di Syrian hamster

L'RNA totale estratto dal bulbo olfattivo è stato utilizzato per costruire librerie di cDNA, in accordo con le istruzioni dei produttori (TruSeq Stranded mRNA sample prep kit, Illumina). Il sequenziatore Illumina NextSeq 500 è stato utilizzato per sequenziare le librerie.

3. Risultati

3.1 Rilevazione di SARS-CoV-2 nella mucosa olfattiva dei pazienti con COVID-19 che mostrano perdita di olfatto

Sono stati analizzati sette pazienti che presentavano, come sintomo principale, una perdita delle funzioni olfattive, gustative, e almeno un sintomo appartenente allo spettro clinico del COVID-19. Il tempo intercorso tra la comparsa dei primi sintomi e l'inclusione nello studio, va da 0 a 13 giorni. A questi sette pazienti sono stati aggiunti quattro controlli sani. L'obiettivo primario della ricerca è stato identificare la presenza di un collegamento tra l'infezione nella mucosa olfattiva e la perdita delle funzioni olfattive. Tutti i pazienti, ma nessuno dei controlli, presentavano RNA di *SARS-CoV-2* a livello di OE, confermando la diagnosi di infezione. Per verificare la presenza di un'attiva replicazione del genoma virale, è stata eseguita un'analisi comparativa del numero di copie genomiche e sub-genomiche (porzioni di RNA ottenute dalla trascrizione del genoma virale, codificanti proteine virali coinvolte nella replicazione, nell'assemblaggio e nella diffusione del virus all'interno dell'ospite), tramite RT-qPCR, confermando che il virus è presente nella mucosa dei pazienti anosmici in attiva replicazione. I tamponi, analizzati mediante immunofluorescenza, sono risultati contenere una quantità variabile di cellule appartenenti all'OE. L'utilizzo dei marcatori OMP (*Olfactory Marker Protein*), per OSN maturi, e PGP9.5 (*Protein Gene Product 9.5*), per tutte le tipologie di neuroni, ha dimostrato la validità della procedura di campionamento (Fig. 2). Inoltre, è stata rilevata la presenza di antigeni di *SARS-CoV-2* (tramite rilevazione della nucleoproteina, NP) e di cellule Iba1$^+$, marcatore

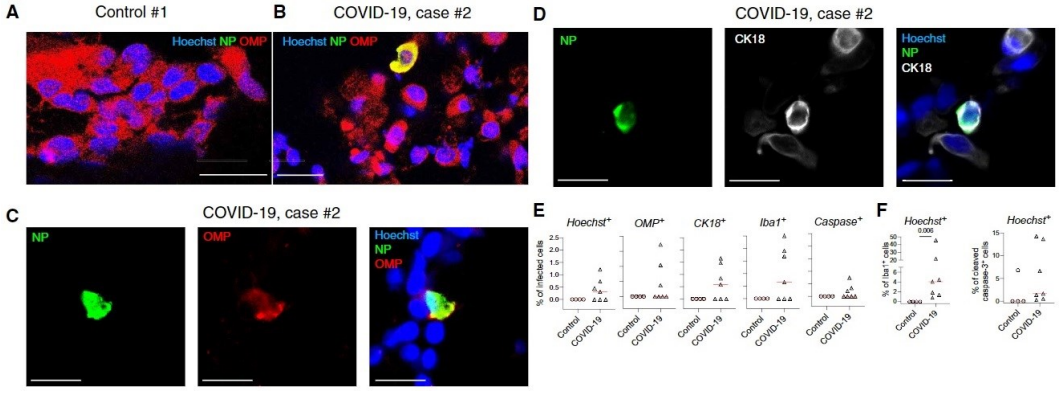

Figura 2. (**A**) Immunofluorescenza di cellule di mucosa olfattiva del controllo #1. (**B**) Cellule di mucosa olfattiva del caso #2. (**C** e **D**) Close-up di immagini di immunofluorescenza di campioni di OE del caso #2. Possiamo vedere OSN maturi infetti (OMP$^+$) (B e C) a fianco di OSC CK18$^+$. (**E**) Percentuale di cellule infettate (NP$^+$) tra le seguenti: Hoechst$^+$, OMP$^+$, CK18$^+$, Iba1$^+$, caspasi-3 clivata$^+$. (**F**) Percentuale di cellule Iba1$^+$ tra le Hoechst$^+$ (sinistra) e percentuale di cellule caspasi-3 clivata$^+$ tra le Hoechst$^+$ (destra). SARS-CoV-2 è rilevato da anticorpi contro la nucleoproteina virale (NP). n = 4 controlli, n = 7 pazienti con COVID-19 (E ed F). Le linee rosse orizzontali indicano le mediane. Scala 20 µm (A e B) o 10 µm (C e D).

con azioni sia pro-infiammatorie che antinfiammatorie, *Ccl5* (*C-C Motif Chemokine Ligand 5*), chemochina pro-infiammatoria, *Isg20* (*Interferon Stimulated Exonuclease Gene 20*), coinvolto nella difesa dall'invasione di virus e *Mx1* (*MX Dynamin Like GTPase 1*), coinvolto nella risposta cellulare antivirale. È emerso che *Cxcl10* risultava elevato nella mucosa olfattiva di gran parte dei pazienti infetti se comparato con i pazienti di controllo, mentre è emersa una variabilità interindividuale sia negli individui infetti che nei controlli per i geni restanti. Questo suggerisce che *SARS-CoV-2* possegga un tropismo per l'OE e che

l'infezione presente sia associata ad un aumento dell'infiammazione locale.

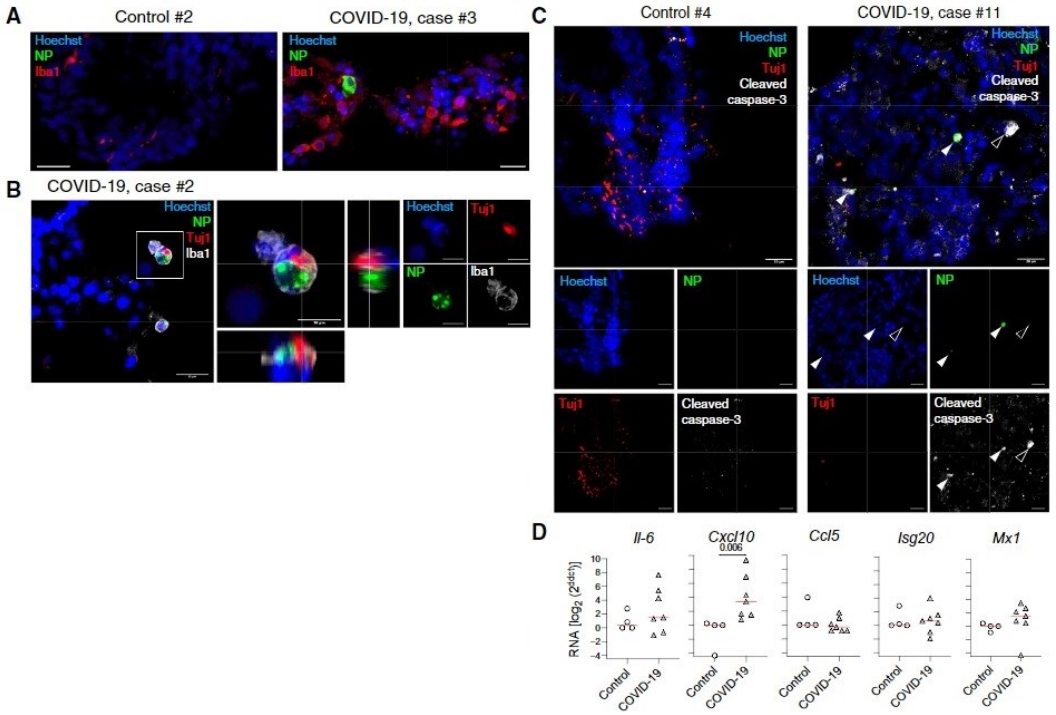

Figura 3. (**A**) Immunofluorescenza di cellule mieloidi (Iba1$^+$) del paziente di controllo #2 confrontato con il caso #3. (**B**) Proiezione ortogonale di antigeni Tuj1$^+$ inclusi in cellule infette Iba1$^+$. (**C**) Immunofluorescenza di cellule apoptotiche (caspasi-3 digerita$^+$) del controllo #4 e del caso #11. Le punte di freccia piene indicano cellule infette positive per caspasi-3 digerita, quelle vuote indicano cellule non infette positive per caspasi-3 digerita. (**D**) Trascritti a livello di mucosa olfattiva di citochine e chemochine. n = 4 controlli, n = 7 pazienti con COVID-19. Le linee orizzontali indicano la mediana. Scala 20 µm (A e B) o 10 µm (C e D).

Successivamente, si è passato all'individuazione delle tipologie di cellule target di *SARS-CoV-2*: sono stati rilevati OSN maturi e immaturi infetti da *SARS-CoV-2* (esprimenti NP), così come OSC (esprimenti CK18, *Caspase-Cleaved Cytokeratin 18*, presente nel plasma in seguito a morte cellulare; Fig. 2, D ed E) e cellule mieloidi (Iba1$^+$; Fig. 2E e 3B). Alcuni degli OSN immaturi infetti, stavano venendo fagocitati dal sistema immunitario. Ulteriori fissazioni contro caspasi-3 digerita sono state poi attuate per verificare se fosse l'infezione ad indurre la morte cellulare nell'OE. Un forte segnale di caspasi-3 digerita è stato rilevato sia nelle cellule infette che in quelle non infette di pazienti con COVID-19, mentre non è stato rilevato nessun segnale dai campioni prelevati dagli individui di controllo. La marcatura, assieme all'osservazione riguardante gli OSN fatta in precedenza, ha mostrato come una gran varietà di tipi cellulari a livello di OE venga infettata da *SARS-CoV-2*, portando ad un aumento di morte cellulare per apoptosi. Tra queste, la perdita di OSN maturi potrebbe essere rilevante nel contesto dell'anosmia.

3.2 Studio della perdita di gusto e olfatto nei criceti infettati da SARS-CoV-2

Con l'obiettivo di valutare l'impatto dell'infezione di *SARS-CoV-2* a livello di sistema olfattivo e strutture cerebrali, criceti di entrambi i sessi sono stati infettati, per via intranasale, con *SARS-CoV-2* e successivamente tenuti in osservazione a partire da 2 dpi fino a 14 dpi. A partire da 2 dpi, sono state rilevate tracce di RNA virale in varie parti del cervello (bulbo olfattivo, corteccia cerebrale, tronco encefalico e cervelletto; Fig. 4, D ed E) e a livello dei turbinati (Fig. 4 C ed E). Dalle stesse zone è stato inoltre possibile isolare particelle infettive virali, dimostrando quindi una replicazione attiva di *SARS-CoV-2* a livello di SNC

(*Sistema Nervoso Centrale*) dei criceti. Successivamente, sono state verificate le

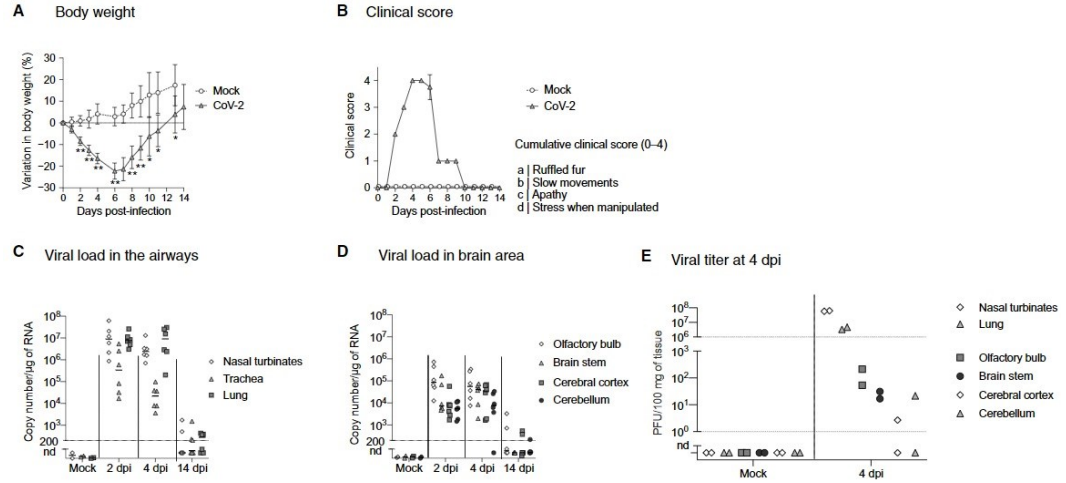

Figura 4. Caratteristiche cliniche e molecolari dell'infezione sperimentale con SARS-CoV-2 in criceto siriano. (**A** e **B**) Variazione in peso corporeo (A) e punteggio clinico (B) di criceti infetti e di controllo per 14 dpi. (**C** e **D**) Quantificazione RNA di SARS-CoV-2 nelle vie aeree di criceto (C) e in differenti aree del cervello (D) degli animali infetti e di controllo a 2, 4 e 14 dpi. (**E**) Titolazione virale infettiva in turbinati nasali, polmoni, bulbo olfattivo, tronco encefalico, corteccia cerebrale e cervelletto a 4 dpi espresso in PFU/100 mg di tessuto. Le linee orizzontali indicano le mediane. n = da 4 a 8 per time point in (A) e (B); n = 6 per time point in (C) e (D); n = 2 per time point in (E).

funzioni olfattive e gustative dei criceti durante il decorso della malattia: a 2 dpi, i criceti sono stati sottoposti ad un test di preferenza del saccarosio, gli individui di controllo hanno dimostrato una chiara preferenza nei confronti dell'acqua addizionata con saccarosio, mentre i criceti infetti non hanno dimostrato nessuna preferenza (Fig. 5A), confermando così la diagnosi di disgeusia o ageusia. Gli stessi criceti sono poi stati sottoposti ad esperimenti di ricerca del cibo: gli individui infetti hanno richiesto più tempo per trovare il cibo nascosto (sotterrato) rispetto ai criceti sani, o non erano in grado di trovarlo (Fig. 5, B e C). Ciononostante, tutti i criceti sono stati in grado di individuare il cibo quando visibile (Fig. 5C), dimostrando che il mancato ritrovamento del cibo sotterrato non era dovuto a deficit locomotori o impedimenti visivi, ma a disturbi olfattivi. Al termine della malattia, quando peso e punteggio clinico sono tornati alla normalità (14 dpi; Fig. 4, A e B), tutti i criceti sono risultati in grado di portare a termine gli stessi test fatti in precedenza, dimostrando una guarigione spontanea dell'anosmia associata all'infezione in questo modello animale.

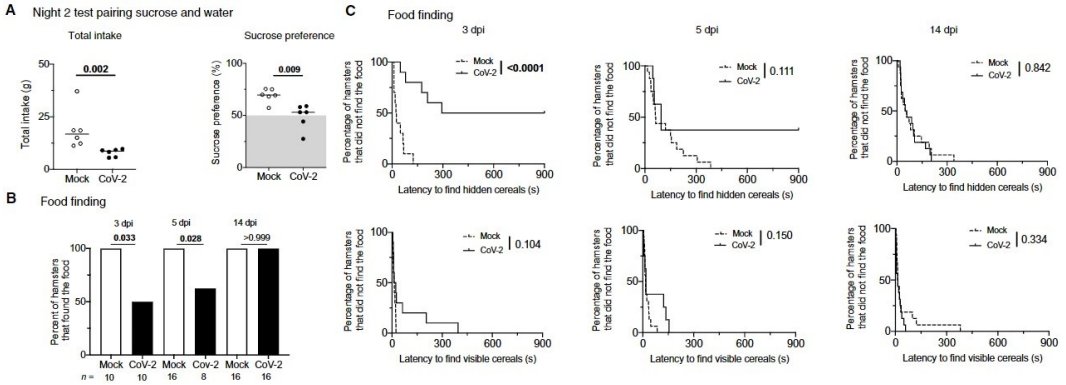

Figura 5. L'infezione con SARS-CoV-2 in criceto induce anosmia e ageusia transienti. (**A**) Variazione del consumo totale di liquidi durante la notte e preferenza nei confronti dell'acqua contenente saccarosio 2% dei criceti infetti e di controllo a 2 dpi. (**B**) Frazione di criceti di controllo o infetti in grado di trovare il cibo nascosto in 15 min. (**C**) Frazione di criceti di controllo o infetti in grado di trovare cibo visibile o nascosto nel tempo. I test di ricerca del cibo sono stati effettuati a 3, 5 e 14 dpi.

3.3 SARS-CoV-2 promuove danni cellulari nell'OE dei criceti infetti

Analisi al SEM dell'OE hanno mostrato un'importante perdita di ciglia in larghe porzioni della superficie epiteliale. A partire da 2 dpi (Fig. 6) fino a 4 dpi, sono state rilevate particelle virali in gemmazione da cellule che avevano perso le

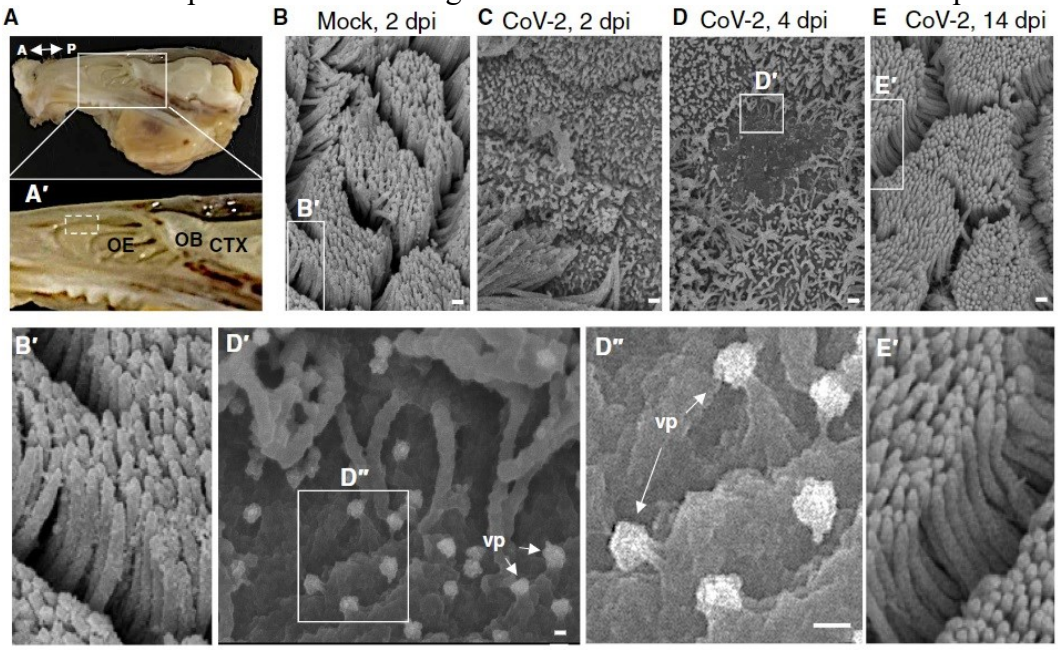

Figura 6. (**A**) testa dissezionata di criceto priva di pelle e mandibola tagliata sagittalmente a metà. La freccia a due punte indica l'asse anteroposteriore (A-P). (**A'**) close-up che mostra la stretta vicinanza tra OE, bulbo olfattivo (OB) e corteccia cerebrale (CTX). Il riquadro tratteggiato indica l'area raccolta per l'analisi al SEM. (da **B** ad **E**) Immagini al SEM che mostrano cambiamenti a livello di OE in seguito a infezione da SARS-CoV-2. L'OE dei criceti di controllo (B e B') e di quelli inoculati con CoV-2 a 2 dpi (C), 4 dpi (D, D' e D"), e 14 dpi (E e E'). Possiamo osservare perdita di ciglia a 2 e 4 dpi nei criceti infetti. Vediamo particelle virali (vp) emergenti dalle cellule deciliate (D' e D", frecce bianche).

ciglia. A 14 dpi, la mucosa olfattiva è apparsa nuovamente ciliata, indistinguibile da quella degli individui di controllo. A 4 dpi sono state rilevate tracce di *SARS-CoV-2* e di un'infiltrazione di cellule mieloidi Iba1^{+}, alcune delle quali risultate positive a *SARS-CoV-2*, segno di una potenziale infezione secondaria dovuta alla fagocitosi di cellule infette (Fig. 7D, la freccia, e Fig. 7J). Sono stati rilevati antigeni di *SARS-CoV-2* nel citoplasma di OSN maturi e immaturi (Fig. 7, A, B, C, D e J) e in quelli delle OSC. Come osservato nei campioni umani, l'infezione induce la morte cellulare, confermata dalla positività a caspasi-3 digerita in cellule neuronali e non (Fig. 7J). Ciò è indice del fatto che la morte cellulare non è causata solo da effetti citopatici di *SARS-CoV-2*, ma probabilmente anche dall'infiammazione locale e dalla risposta immunitaria all'infezione.

3.4 Disseminazione di SARS-CoV-2 nel cervello e neuroinfiammazione in criceti infetti

Il quesito successivo è se *SARS-CoV-2* possa invadere il SNC attraverso la via retrograda a partire dal sistema olfattivo. *SARS-CoV-2* è stato rilevato a livello di fasci di nervi olfattivi e nella giunzione che collega nervo olfattivo e bulbo olfattivo, ma anche a livello di assoni di OSN che raggiungono il bulbo olfattivo (Fig. 7). Ciò suggerisce che *SARS-CoV-2* possa arrivare al cervello attraverso il sistema olfattivo per via retrograda, pur non escludendo altre alternative. A conferma di ciò, a livello dei turbinati nasali, è stata rilevata una sovraespressione dei geni *IL-6*, *Cxcl10*, *Ifn-β* (*Interferone-β*), *Ifn-λ* (*Interferone-λ*), e *Il-1β* (*Interleuchina-1β*, citochina pro-infiammatoria), coinvolti nella risposta

infiammatoria, a 2 dpi, e un leggero aumento di questa a 4 e 14 dpi. In maniera simile, ma con tempistica ritardata, il bulbo olfattivo presenta una sovraespressione degli stessi geni (Fig. 7N). Attraverso RNA-seq è stata osservata una serie di Geni Differenzialmente Espressi (DEG) (Fig. 8), rispettivamente 374 *up*-regolati e 51 *down*-regolati a livello di bulbo olfattivo di criceti infetti a 4 dpi (Fig. 8 A). I DEG sono stati classificati in accordo con il *pathway* KEGG (Kyoto Encyclopedia of Genes and Genomes) e i termini GO (Gene Ontology) sulla base dei loro processi biologici, sulle funzioni molecolari e sui componenti cellulari. I geni *up*-regolati erano principalmente coinvolti nella risposta infiammatoria e nelle risposte a infezione da virus, con componenti dell'immunità innata [come, ad esempio, la risposta mediata da interferone di tipo I (IFN), attivazione delle cellule natural killer, Toll-Like Receptors (TLR)], dell'immunità adattativa [cellule T helper (T_H1, T_H2) e cellule T $CD4^+$], funzioni collegate alla segnalazione da parte di chemochine, e regolazioni di processi quali i *pathway* di segnalazione dei TLR e quelli di regolazione delle cellule T helper. Per validare il coinvolgimento di questi *pathways* di segnalazione provocati dall'*up*-regolazione dei DEG, è stata effettuata un'analisi per qRT-PCR di geni caratteristici del bulbo olfattivo che ha confermato una sovraespressione dei geni *Mx2* (*MX Dynamin Like GTPase 2*), *Irf7* (*Interferon Regulatory Factor 7*), *Ddx58* (*DExH-Box Helicase 58*) e *Stat1* (*Signal Transducer and Activator of Transcription 1*) tra i 2 e i 4 dpi, mentre *Ccl5* risultava sovraespressa solo a partire da 4 dpi. Trattandosi di geni coinvolti nella risposta infiammatoria, la loro *up*-regolazione supporta l'ipotesi che la neuroinvasione di *SARS-CoV-2* porti a neuroinfiammazione. Una sovraespressione di *Cxcl10*, *Il-1β*, *Ccl5* e *Irf7* fino a 14 dpi, quando gli animali erano ormai guariti da ageusia/anosmia, indica, inoltre, la persistenza di un processo infiammatorio infettivo/post-infettivo anche nella fase asintomatica o post-sintomatica nell'organismo modello.

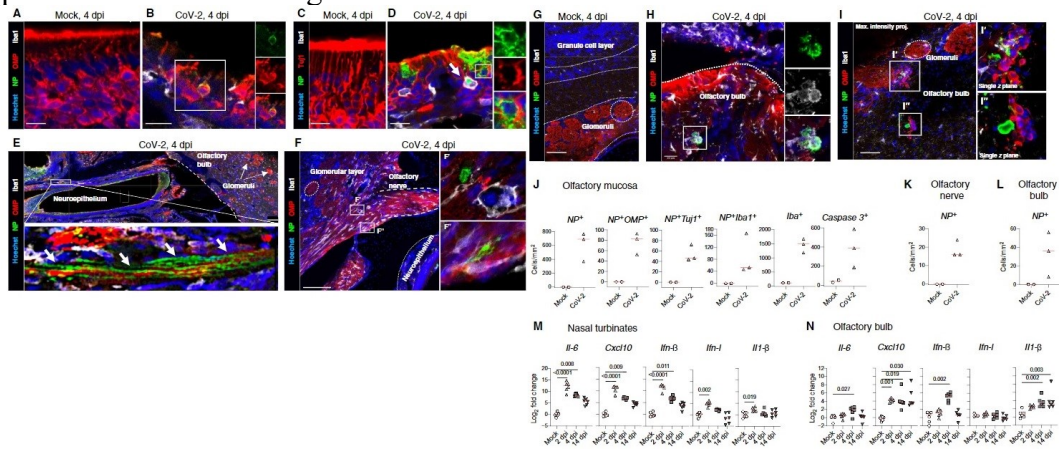

Figura 7. Rilevazione di antigeni di SARS-CoV-2 e quantificazione dei livelli di espressione di citochine/chemochine nel sistema olfattivo di criceto. (da **A** a **D**) Epitelio olfattivo di controlli (A e C) e criceti infetti (B e D) a 4 dpi. I riquadri mostrano OSN maturi infetti OMP^+ (B) o OSN immaturi infetti $Tuj1^+$ (D). La freccia in (D) indica una cellula infetta $Iba1^+$. (**E**) Sezione sagittale di turbinati nasali e bulbo olfattivo di criceti infetti a 4 dpi. I riquadri raffigurano staining di SARS-CoV-2 in assoni di OSN. (**F**) Assoni sensoriali olfattivi si proiettano nel glomerulo nel bulbo olfattivo di criceti infetti a 4 dpi. I riquadri (F' e F") mostrano cellule infette. (da **G** a **I**) Bulbo olfattivo di controlli (G) e criceti infetti (H e I) a 4 dpi. Cellule infette $Iba1^+$ in (H e I). SARS-CoV-2 è rilevato da anticorpi contro la NP virale. Scala 20 µm (da A a D e H), 100 µm (E ed F), e 50 µm (G e I). le immagini sono singoli piani Z (da A ad H) o una proiezione a massima intensità su una profondità di 6 µm (I). (**J**) Numero di cellule NP^+, NP^+ OMP^+, NP^+ $Tuj1^+$, NP^+ $Iba1^+$, $Iba1^+$ e caspasi-3 clivata$^+$ nella mucosa olfattiva. (**K** e **L**) Numero di cellule NP^+ nel nervo olfattivo (K) e nel bulbo olfattivo (L). (**M** e **N**) Trascritti di citochine e chemochine nei turbinati nasali (M) e nel bulbo olfattivo (N) a 2, 4 e 14 dpi.

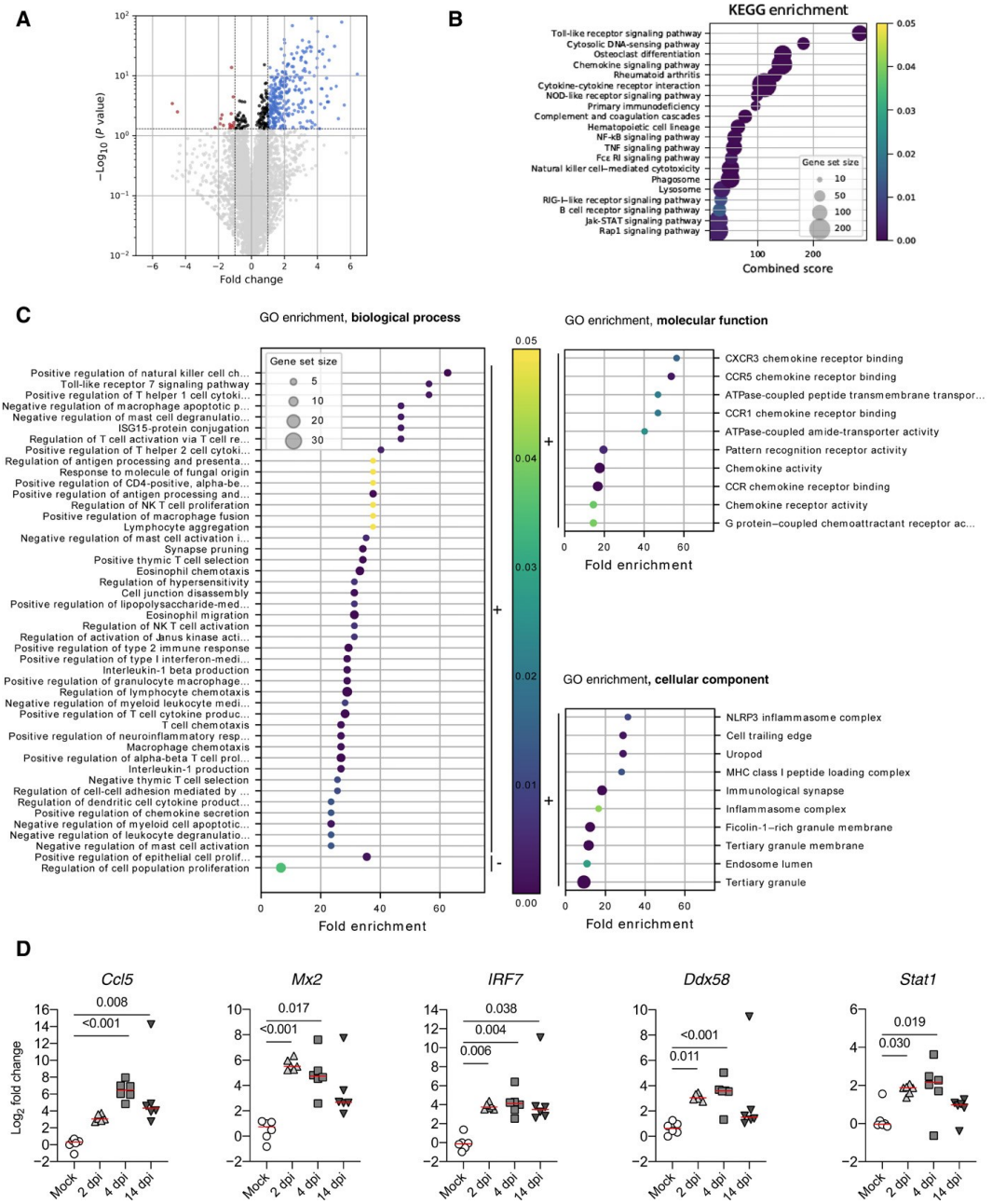

Figura 8. DEG nel bulbo olfattivo di criceti infetti da SARS-CoV-2 (a 4 dpi) ottenuti da RNA-seq. (**A**) Grafico a vulcano ottenuto dal confronto tra campioni infetti e controlli sani. I punti grigi rappresentano i geni che non superano una soglia di *False Discovery Rate* (FDR) < 0.05. I punti neri rappresentano i geni che superano la soglia di FDR, ma con un *fold change* tra -1 e 1. I punti rossi e blu corrispondono a DEG sotto- e sovraespressi con un fold change rispettivamente inferiore a -1 o superiore a 1. (**B**) Arricchimento dei *pathway* KEGG basato sui DEG tra campioni infetti e controllo. Il diametro dei cerchi è proporzionale al numero di geni che fanno parte del *pathway*. Il colore cel cerchio è proporzionale ai *P-value* corretti e corrisponde alla scala presentata in (C) e (D). (**C**) Analisi di GO considerando i processi biologici. Le barre nere nel lato destro del grafico a dispersione indicano un arricchimento basato su set di geni up-regolati ("+") e down-regolati ("-"). Il diametro dei cerchi è proporzionale al numero di geni che fanno parte del processo biologico rappresentato. Il colore del cerchio è proporzionale ai *P-value* corretti e corrisponde alla scala presentata in (C) e (D). (**D**) Livello di espressione dei geni *Ccl5, Mx2, IRF7, Ddx58* e *Stat1* nel bulbo olfattivo a 2, 4 e 14 dpi. n = 6 per *time point*. Il *P-value* è indicato dove significativo. Le linee orizzontali indicano le mediane.

4. Discussione

La perdita di gusto e olfatto causate dall'infezione di *SARS-CoV-2* sono frequenti nei pazienti COVID-19. Per questo motivo, sono state fatte diverse ipotesi che potessero spiegare l'insorgenza di anosmia ed ageusia in seguito all'infezione virale. In questo studio, si è ipotizzato che la causa possa essere correlata al danneggiamento dell'OE e/o alla morte cellulare dei OSN. Le prime analisi effettuate hanno confermato la presenza di *SARS-CoV-2* in tutti i pazienti che presentavano anosmia e dimostrato un'attiva replicazione virale a livello dell'OE. L'infezione causata da *SARS-CoV-2* è correlata ad un'infiammazione a livello dell'OE, ipotesi sostenuta dalla rilevazione di cellule adibite alla risposta immunitaria ($Iba1^{+}$) e all'individuazione di un'elevata espressione di citochine e mediatori dell'infiammazione. Si è successivamente analizzato quali tipologie cellulari fossero soggette a infezione da parte del virus ed è stato osservato che OSN maturi e immaturi, OSC e cellule mieloidi sono risultate positive a *SARS-CoV-2*. È stato rilevato un forte segnale di cellule positive a caspasi-3 digerita nei campioni di pazienti infettati, mentre non è stato rilevato alcun segnale a livello dei pazienti di controllo, confermando che è l'infezione da *SARS-CoV-2* a provocare la morte cellulare. Per via delle limitazioni riguardanti le analisi effettuabili in uomo, che non hanno permesso campionamenti troppo invasivi della mucosa olfattiva, gli stessi esperimenti sono stati effettuati in criceto, modello per la patologia causata da *SARS-CoV-2*. È stato confermato che l'infezione è presente nell'OE dei criceti e ha come *target* le stesse tipologie cellulari rilevate in uomo, e che l'infezione è accompagnata da un'infiammazione locale e morte cellulare. Analisi di microscopia a scansione di tessuti dell'OE,

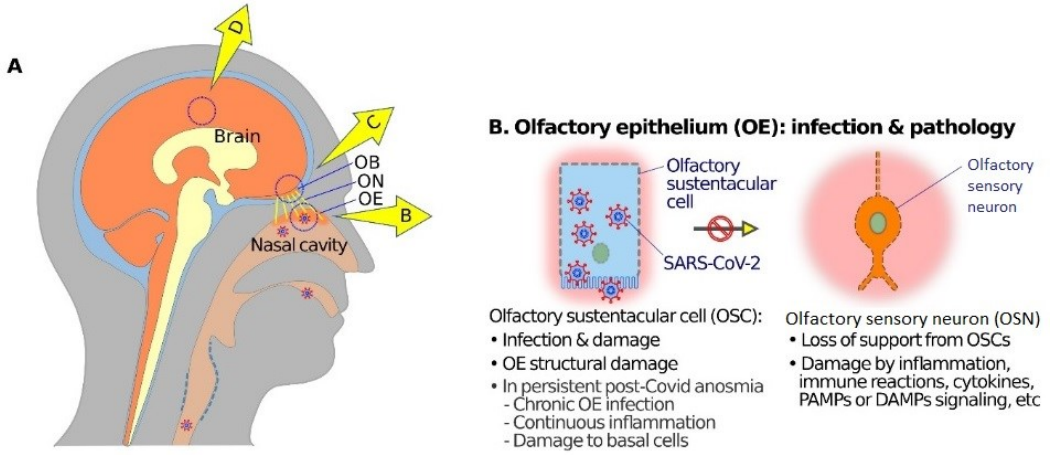

Figura 9. Schema esplicativo del possibile meccanismo della neuropatogenesi olfattiva di COVID-19. (**A**) Schema che illustra le relazioni tra cavità nasale, OE, nervo olfattivo (OV), bulbo olfattivo (OB), e il cervello. (**B**) secondo lo studio di Liang e colleghi, a livello di OE, SARS-CoV-2 infetta principalmente OSC dato l'alto livello di espressione di ACE2 sulla superficie. L'infezione delle OSC e il loro danneggiamento può portare a infiammazione, reazioni immunitarie, rilascio di citochine.

hanno rilevato un'importante perdita di ciglia in larghe aree dell'epitelio, le quali sono risultate altamente disorganizzate e presentavano particelle virali in gemmazione. È, inoltre, stata rilevata la presenza di alcuni OSN infetti in apoptosi. È stato verificato che l'infezione è in grado di raggiungere il cervello, grazie al rilevamento di RNA virale a livello di bulbo olfattivo. Una volta terminato il decorso della malattia, quando i criceti risultavano possedere tutte le funzionalità olfattive e gustative, è stato osservato che l'OE è nuovamente ciliato e ordinato. L'insieme dei dati ottenuti sembra confermare l'ipotesi iniziale che

suggeriva che l'insorgenza dell'anosmia fosse dovuta a un danneggiamento a livello di OE e/o dalla morte dei OSN. Non essendo ancora del tutto chiaro il meccanismo di infezione causato da *SARS-CoV-2*, sono stati effettuati molti studi che cercavano di spiegare le dinamiche alla base dell'anosmia causata da COVID-19. Alcuni di questi hanno sostenuto l'ipotesi che vedeva come causa principale il danneggiamento dell'OE. Uno studio pubblicato da Bryche e colleghi, ad esempio, basato sull'inoculazione di *SARS-CoV-2* in criceto siriano ha dimostrato una forte disorganizzazione a livello di OE, caratterizzata dalla presenza di aggregati cellulari e l'esposizione degli assoni di OSN all'ambiente esterno (Bryche, 2020). Ulteriori studi hanno poi portato a mostrare come l'infezione a livello dell'OE avvenga tramite OSC, le quali sembrano presentare la più alta espressione di ACE2 (Liang, 2021). Non è ancora del tutto chiaro se i OSN possano essere infettati direttamente da *SARS-CoV-2*, nonostante molti degli studi portino a pensare che l'infezione avvenga principalmente a livello di cellule non neuronali (Liang, 2021). Essendo le OSC cellule adibite al sostentamento strutturale e metabolico dei OSN, e quindi cellule essenziali a livello di OE, l'infezione a livello di queste cellule si ripercuote poi anche a livello di tutto l'OE (Fig. 9), portando quindi a: perdita di ciglia a livello di OSN, infiltrazione di cellule del sistema immunitario e morte cellulare. Questi studi esprimono, quindi, pareri discordanti per quanto riguarda l'infezione di OSN da parte di *SARS-CoV-2*. Nonostante lo studio esaminato riporti la possibilità di infezione di OSN da parte di *SARS-CoV-2*, specifica anche che non è tutt'ora chiaro se l'infezione sia diretta o se possa trattarsi di un'infezione secondaria dovuta alla diffusione del virus di cellula in cellula. Altri studi invece riportano come sia quasi o totalmente assente la presenza di OSN infetti (Liang, 2021). Tutti questi studi concordano sul fatto che l'anosmia è probabilmente causata da danni a livello di OE, seppur con meccanismi diversi. È plausibile, quindi, pensare che i danni a livello olfattivo possano essere dovuti al danneggiamento dell'OE, attraverso la perdita di ciglia, e il danneggiamento o la morte dei OSN, i quali sono i responsabili della percezione dell'olfatto. Appare chiaro, inoltre, come le OSC svolgano un ruolo nell'infezione da *SARS-CoV-2*, permettendo l'ingresso del virus a livello di OE e portando a un'infiammazione. Comprendere appieno il meccanismo che sta alla base dell'anosmia, quindi, può fornire un ulteriore passo avanti per quanto riguarda il trattamento di pazienti che presentano deficit olfattivi e gustativi che possono persistere anche in seguito a guarigione dalla malattia, permettendo quindi il recupero delle totali abilità olfattive. Analizzando gli esperimenti e le procedure effettuate per questo studio, ho identificato alcuni aspetti critici del lavoro. Il numero di pazienti analizzati, ad esempio, è limitato e non bilanciato con il numero di individui sani reclutati. I prelievi fatti a livello di OE, sono una parte essenziale dello studio. Tuttavia, il corretto prelievo è stato validato solamente mediante la rilevazione di marcatori specifici per OSN, e nessun altro marcatore che avesse come target altre tipologie cellulari presenti a livello di OE. L'aggiunta di ulteriori marker, quindi, avrebbe portato ad una maggior sicurezza nel metodo di prelievo delle biopsie, poiché l'utilizzo di marcatori specifici solo per le cellule neuronali potrebbe non portare alla luce problemi riguardanti l'esecuzione del campionamento, come ad esempio un campionamento parziale dell'OE, e/o il campionamento di una porzione errata di tessuto rispetto a quella di nostro interesse.

Bibliografia

de Melo GD, Lazarini F, Levallois S, Hautefort C, Michel V, Larrous F, Verillaud B, Aparicio C, Wagner S, Gheusi G, Kergoat L, Kornobis E, Donati F, Cokelaer T, Hervochon R, Madec Y, Roze E, Salmon D, Bourhy H, Lecuit M, Lledo PM (2021). COVID-19-related anosmia is associated with viral persistence and inflammation in human olfactory epithelium and brain infection in hamsters. *Sci Transl Med*. **13**(596):eabf8396.

Gruber AD, Firsching TC, Trimpert J, Dietert K (2022). Hamster models of COVID-19 pneumonia reviewed: How human can they be? *Vet Pathol.* **59**(4):528-545.

Robert Hubrecht, James Kirkwood (2010). The UFAW Handbook on the Care and Management of Laboratory and Other Research Animals. (8th edition), Wiley-Blackwell.

Koyama S, Kondo K, Ueha R, Kashiwadani H, Heinbockel T (2021). Possible Use of Phytochemicals for Recovery from COVID-19-Induced Anosmia and Ageusia. *Int J Mol Sci.* **22**(16):8912.

Liang F (2020). Sustentacular Cell Enwrapment of Olfactory Receptor Neuronal Dendrites: An Update. *Genes (Basel).* 30;11(5):493.

Muñoz-Fontela C, Dowling WE, Funnell SGP, Gsell PS, Riveros-Balta AX, Albrecht RA, Andersen H, Baric RS, Carroll MW, Cavaleri M, Qin C, Crozier I, Dallmeier K, de Waal L, de Wit E, Delang L, Dohm E, Duprex WP, Falzarano D, Finch CL, Frieman MB, Graham BS, Gralinski LE, Guilfoyle K, Haagmans BL, Hamilton GA, Hartman AL, Herfst S, Kaptein SJF, Klimstra WB, Knezevic I, Krause PR, Kuhn JH, Le Grand R, Lewis MG, Liu WC, Maisonnasse P, McElroy AK, Munster V, Oreshkova N, Rasmussen AL, Rocha-Pereira J, Rockx B, Rodríguez E, Rogers TF, Salguero FJ, Schotsaert M, Stittelaar KJ, Thibaut HJ, Tseng CT, Vergara-Alert J, Beer M, Brasel T, Chan JFW, García-Sastre A, Neyts J, Perlman S, Reed DS, Richt JA, Roy CJ, Segalés J, Vasan SS, Henao-Restrepo AM, Barouch DH (2020). Animal models for COVID-19. *Nature*. **586**(7830):509-515.

Ochani R, Asad A, Yasmin F, Shaikh S, Khalid H, Batra S, Sohail MR, Mahmood SF, Ochani R, Hussham Arshad M, Kumar A, Surani S (2021). COVID-19 pandemic: from origins to outcomes. A comprehensive review of viral pathogenesis, clinical manifestations, diagnostic evaluation, and management. *Infez Med.* **29**(1):20-36.

Bryche B, St Albin A, Murri S, Lacôte S, Pulido C, Ar Gouilh M, Lesellier S, Servat A, Wasniewski M, Picard-Meyer E, Monchatre-Leroy E, Volmer R, Rampin O, Le Goffic R, Marianneau P, Meunier N (2020). Massive transient damage of the olfactory epithelium associated with infection of sustentacular cells by SARS-CoV-2 in golden Syrian hamsters. *Brain Behav Immun*. **89**:579-586.

Liang F, Wang Y (2021). COVID-19 Anosmia: High Prevalence, Plural Neuropathogenic Mechanisms, and Scarce Neurotropism of SARS-CoV-2? *Viruses*.**13**(11):2225.

CORONAVIRUS

COVID-19–related anosmia is associated with viral persistence and inflammation in human olfactory epithelium and brain infection in hamsters

Guilherme Dias de Melo[1†], Françoise Lazarini[2†], Sylvain Levallois[3,4†], Charlotte Hautefort[5†], Vincent Michel[2,6,7], Florence Larrous[1], Benjamin Verillaud[5], Caroline Aparicio[8], Sebastien Wagner[2], Gilles Gheusi[2,9], Lauriane Kergoat[1], Etienne Kornobis[10,11], Flora Donati[12,13], Thomas Cokelaer[10,11], Rémi Hervochon[14], Yoann Madec[15], Emmanuel Roze[16], Dominique Salmon[17], Hervé Bourhy[1‡], Marc Lecuit[3,4,18‡], Pierre-Marie Lledo[2*‡]

Whereas recent investigations have revealed viral, inflammatory, and vascular factors involved in severe acute respiratory syndrome coronavirus 2 (SARS-CoV-2) lung pathogenesis, the pathophysiology of neurological disorders in coronavirus disease 2019 (COVID-19) remains poorly understood. Olfactory and taste dysfunction are common in COVID-19, especially in mildly symptomatic patients. Here, we conducted a virologic, molecular, and cellular study of the olfactory neuroepithelium of seven patients with COVID-19 presenting with acute loss of smell. We report evidence that the olfactory neuroepithelium is a major site of SARS-CoV2 infection with multiple cell types, including olfactory sensory neurons, support cells, and immune cells, becoming infected. SARS-CoV-2 replication in the olfactory neuroepithelium was associated with local inflammation. Furthermore, we showed that SARS-CoV-2 induced acute anosmia and ageusia in golden Syrian hamsters, lasting as long as the virus remained in the olfactory epithelium and the olfactory bulb. Last, olfactory mucosa sampling from patients showing long-term persistence of COVID-19–associated anosmia revealed the presence of virus transcripts and of SARS-CoV-2–infected cells, together with protracted inflammation. SARS-CoV-2 persistence and associated inflammation in the olfactory neuroepithelium may account for prolonged or relapsing symptoms of COVID-19, such as loss of smell, which should be considered for optimal medical management of this disease.

INTRODUCTION

Coronavirus disease 2019 (COVID-19), caused by severe acute respiratory syndrome coronavirus 2 (SARS-CoV-2), commonly induces airway and pulmonary symptoms and, in severe cases, leads to respiratory distress and death (*1*). Although COVID-19 is primarily a respiratory disease, many patients exhibit extrarespiratory symptoms of various severity. Among these, a sudden loss of olfactory function in SARS-CoV-2–infected individuals was reported worldwide at the onset of the pandemic. Loss of smell (anosmia) and/or of taste (ageusia) are considered now as cardinal symptoms of COVID-19 (*2*–*4*). Likewise, a wide range of central and peripheral neurological manifestations have been observed in severe patients. Although neuropilin-1 was found to facilitate SARS-CoV-2 entry in neural cells (*5*), and thus a neurotropism of SARS-CoV-2 could be suspected, a direct role of the virus in the neurological manifestations remains highly debated (*2*, *6*).

The bona fide virus entry receptor is the angiotensin-converting enzyme 2 (ACE2), which is expressed along the entire human respiratory system, thereby accounting for SARS-CoV-2 respiratory tropism (*7*, *8*). In the upper airways, and more precisely in the superior-posterior portion of the nasal cavities, resides the olfactory mucosa. This region is where the respiratory tract is in direct contact with the central nervous system (CNS), via olfactory sensory neurons (OSNs), of which cilia emerge within the nasal cavity and their axons project into the olfactory bulb (*9*). Because loss of smell is a hallmark of COVID-19 and several respiratory viruses (influenza, endemic human CoVs, and SARS-CoV-1) invade the CNS through the olfactory mucosa via a retrograde route (*10*), we hypothesized that SARS-CoV-2 might be neurotropic and capable of invading the CNS through OSNs.

SARS-CoV-2 can infect neurons in human brain organoids (*11*), and recent reports have confirmed the presence of SARS-CoV-2 in olfactory mucosa OSNs that express neuropilin-1 (*5*) and deeper within the CNS at autopsy (*12*, *13*). Yet, the portal of entry of SARS-CoV-2 in the CNS remains elusive, as well as the exact mechanism

[1]Lyssavirus Epidemiology and Neuropathology Unit, Institut Pasteur, 75015 Paris, France. [2]Perception and Memory Unit, Institut Pasteur, CNRS UMR3571, 75015 Paris, France. [3]Biology of Infection Unit, Institut Pasteur, 75015 Paris, France. [4]INSERM U1117, 75015 Paris, France. [5] Otolaryngology–Head and Neck Surgery Department, Hopital Lariboisiere, Assistance Publique–Hôpitaux de Paris, INSERM U1141, Université de Paris, 75010 Paris, France. [6]Institut de l'Audition, Institut Pasteur, Paris, France. [7]INSERM U1120, 75012 Paris, France. [8]Emergency Department, Hôpital Lariboisière, Assistance Publique–Hôpitaux de Paris, Université de Paris, 75010 Paris, France. [9]Laboratory of Experimental and Comparative Ethology, Université Sorbonne Paris Nord, Villetaneuse, France. [10]Plateforme Technologique Biomics–Centre de Ressources et Recherches Technologiques (C2RT), Institut Pasteur, 75015 Paris, France. [11]Hub de Bioinformatique et Biostatistique–Département Biologie Computationnelle, Institut Pasteur, USR 3756 CNRS, 75015 Paris, France. [12]National Reference Center for Respiratory Viruses, Institut Pasteur, 75015 Paris, France. [13]Molecular Genetics of RNA Viruses, CNRS UMR3569, University of Paris, Institut Pasteur, 75015 Paris, France. [14]Otolaryngology–Head and Neck Surgery Department, GHU Pitié-Salpêtrière, Assistance Publique–Hôpitaux de Paris, Sorbonne Université, 75013 Paris, France. [15]Emerging Diseases Epidemiology Unit, Institut Pasteur, 75015 Paris, France. [16]Sorbonne Université, AP-HP, Hôpital de la Pitié-Salpêtrière, Département de Neurologie, INSERM U1127, CNRS UMR 7225, Institut du Cerveau, 75013 Paris, France. [17]Infectious Diseases and Immunology Department, Cochin Hotel Dieu Hospital, Assistance Publique–Hôpitaux de Paris, Université de Paris, 75015 Paris, France. [18]Université de Paris, Necker-Enfants Malades University Hospital, Division of Infectious Diseases and Tropical Medicine, Institut Imagine, AP-HP, 75015 Paris, France.
*Corresponding author. Email: pmlledo@pasteur.fr
†These authors contributed equally to this work.
‡These authors share senior authorship.

leading to the olfactory dysfunction in patients with COVID-19. Various hypotheses have been proposed such as conductive loss due to obstruction of the olfactory cleft (*14*), alteration of OSN neurogenesis (*15*), and secondary CNS damage related to edema in the olfactory bulb (*16*, *17*). Detailed study of the olfactory system and olfaction in living patients with COVID-19 is thus needed to investigate the SARS-CoV-2 neuroinvasiveness in the olfactory neuroepithelium.

Complementary to this approach, animal models recapitulating the biological and clinical characteristics of SARS-CoV-2–related anosmia and ageusia would constitute useful tools to address deeper mechanisms. In this regard, wild-type mice are poorly susceptible to SARS-CoV-2 infection because the mouse ACE2 ortholog is not acting as a receptor for this virus (*18*). Moreover, the various transgenic mouse lines expressing the human version of the virus entry receptor (hACE2) under the control of different promoters display disproportionate high CNS infection leading to fatal encephalitis (*19*–*22*), which rarely occurs in patients with COVID-19. This mismatch likely reflects the artefactual ectopic and high expression of hACE2 caused by the different transgene promoters. In contrast, the golden Syrian hamster (*Mesocricetus auratus*) expresses an endogenous ACE2 protein able to interact with SARS-CoV-2 (*18*) and constitutes a naturally permissive model of SARS-CoV-2 infection (*23*–*25*). Previous reports have shown infection in hamster olfactory mucosa, but whether olfactory neurons can be infected or only non-neuronal, epithelial sustentacular cells remains controversial (*26*, *27*). Moreover, the link between infection, inflammation, and tissue disruption of the olfactory neuroepithelium and corresponding brain regions is unclear. Likewise, how damage of the neuroepithelium correlates with anosmia, and the potential SARS-CoV-2 neuroinvasion from the olfactory system to its downstream brain structures, remains highly debated.

Here, we report the interactions of SARS-CoV-2 with the olfactory system and its pathophysiological mechanisms. We first investigated SARS-CoV-2 infection of the olfactory mucosa in patients with COVID-19 and recent loss of smell. Because olfactory mucosa biopsy is an invasive procedure, which cannot be used for research purpose in patients with COVID-19, we performed nasal mucosa brush sampling, a noninvasive technique previously used in patients to study neurodegenerative and infectious diseases (*28*–*30*). We next attempted to model SARS-CoV-2–associated anosmia/ageusia in golden Syrian hamsters to further investigate the pathogenesis of neuroepithelium and CNS infection. Last, we investigated the olfactory mucosa of post–COVID-19 patients presenting long-lasting olfactory dysfunction.

RESULTS

SARS-CoV-2 detection in the olfactory mucosa of patients with COVID-19 exhibiting loss of smell

We enrolled seven patients who were referred to the ear, nose, and throat (ENT) department for olfactory function loss and COVID-19 suspicion in the context of the COVID-19 first wave in Paris, France, alongside with four healthy controls. The main clinical features of patients and controls are listed in tables S1 and S2. The time from first COVID-19–related symptoms to inclusion in the study ranged from 0 to 13 days. None of the patients required hospitalization. Their prominent symptom was recent loss of olfactory function (sudden for six patients but progressive for case #1) and was accompanied with taste changes (except case #3) and at least one symptom belonging to the clinical spectrum of COVID-19, such as diarrhea, cough, dyspnea, conjunctivitis, fever, fatigue, headache, muscle pain, laryngitis, or a sore throat (fig. S1A). Olfactory function loss was the first symptom related to COVID-19 in cases #5 and #14, whereas it was preceded by or concomitant to other symptoms in the remaining patients. Smell loss was deemed severe for cases #1, #2, #4, #5, #14, and #15 and moderate for case #3. Taste loss was deemed severe for cases #1, #2, #4, #5, and #14 and mild for case #15. The characteristics of the taste and smell abnormalities are listed in table S3. Other otolaryngologic symptoms were rhinorrhea for four patients, not concomitant with smell loss; nasal irritation for two patients; and hyperacusis for case #1. Nasal obstruction was not reported in any of the patients. Taste changes were characterized in the six patients with dysgeusia and included reduced acuity for sweet taste, bad taste in the mouth, reduced or increased acuity for bitterness, or reduced acuity for salt or sour. Three patients (#2, #4, and #15) were unable to discriminate between different food flavors such as meat and fish.

To investigate whether infection in the olfactory mucosa was associated with olfactory functional loss, all patients underwent olfactory mucosa brush cytological sampling. Four patients had detectable SARS-CoV-2 RNA, using the conventional nasopharyngeal samples at inclusion (tables S1 and S2). All patients, but none of the controls, had detectable SARS-CoV-2 RNA in cytological samples from the olfactory mucosa using the reverse transcription quantitative polymerase chain reaction (RT-qPCR) SYBR green technique, unambiguously confirming the diagnosis of SARS-CoV-2 infection (tables S1 and S2). To further investigate whether the presence of viral RNA in the olfactory mucosa reflected active replication of SARS-CoV-2 genome, we performed a comparative analysis of genomic and subgenomic copy numbers by RT-qPCR. Patients #2, #14, and #15 exhibited a strong viral genomic RNA load in the olfactory mucosa (2.25×10^6, 8.09×10^7, and 7.17×10^6 RNA copies/μl, respectively), and subgenomic RNA was detected in patient #14 (5.66×10^6 copies/μl), whereas other cases were detected as positive (above the limit of detection with RT-qPCR SYBR green) but not quantifiable (below the limit of quantification, less than 200 RNA copies/μl using the RT-qPCR TaqMan technique) (tables S1 and S2). Given the high viral genomic RNA load in the olfactory mucosa of the patients #14 and #15, we determined the SARS-CoV-2 titer in their olfactory mucosa. Infectious SARS-CoV-2 were isolated from the olfactory mucosa of patients #14 [1.19×10^6 plaque-forming units (PFU)/ml] and #15 (5.38×10^2 PFU/ml) but not in sex- and age-matched controls, indicating that infectious virus is indeed present in the olfactory mucosa of anosmic patients (table S2).

We further investigated the viral presence in the olfactory mucosa by immunofluorescence labeling of the cytological samples. Variable cell density between olfactory mucosa samples from the COVID-19 and control individuals was found, but all samples contained mature OSNs. Cells positive for Olfactory Marker Protein (OMP) and Protein Gene Product 9.5 (PGP9.5) were consistently present, and *OMP* transcripts recovered from all the samples, validating the quality of the swabbing procedure (Fig. 1, A and B; fig. S1B; and tables S1 and S2). Immunostaining revealed the presence of SARS-CoV-2 antigens [nucleoprotein (NP)] in four patients (RT-qPCR$^+$) out of seven but never in controls (tables S1 and S2 and Fig. 1). We observed numerous Iba1$^+$ (immune myeloid) cells in the olfactory mucosa of all patients whereas few to no Iba1$^+$ cells in controls

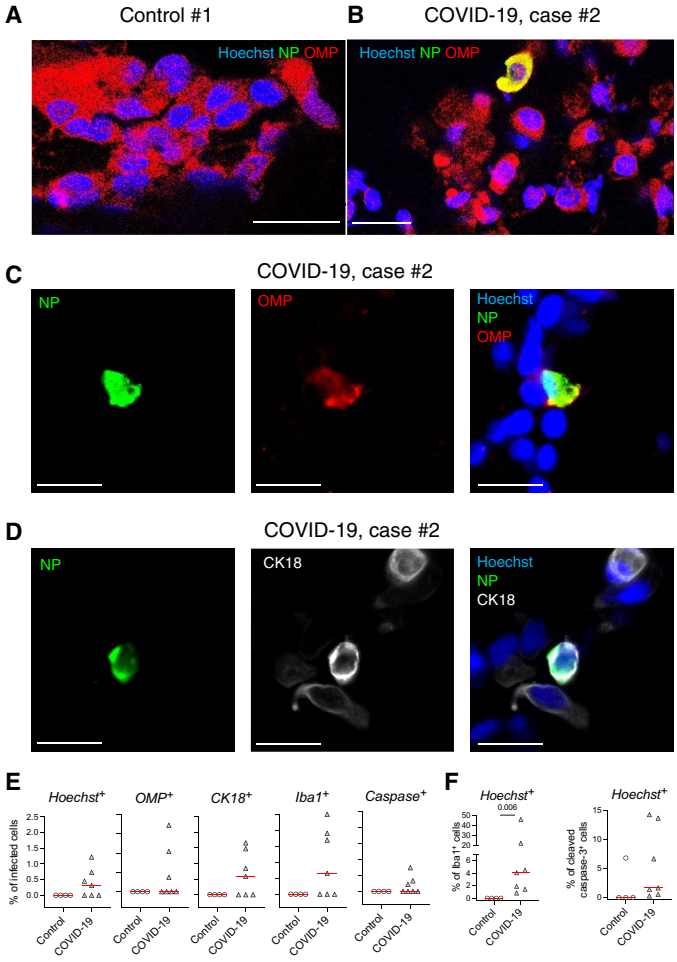

Fig. 1. Analysis of olfactory mucosa from patients with COVID-19 with acute olfactory function loss, at early stage of infection. (**A**) Immunofluorescence of cells retrieved from the olfactory mucosa of the control participant #1. (**B**) Cells retrieved from the olfactory mucosa of case #2. (**C** and **D**) Close-up immunofluorescence images of olfactory epithelium samples from case #2. Infected mature olfactory neurons (OMP$^+$) are observed (B and C), alongside sustentacular CK18$^+$ cells (D). (**E**) Percent of infected (NP$^+$) cells among the following: Hoechst$^+$ cells, OMP$^+$ cells, CK18$^+$ cells, Iba1$^+$ cells, and cleaved caspase-3$^+$ cells. (**F**) Percent of Iba1$^+$ cells among Hoechst$^+$ cells (left) and percent of cleaved caspase-3$^+$ cells among Hoechst$^+$ cells (right). SARS-CoV-2 is detected by antibodies raised against the viral nucleoprotein (NP). $n = 4$ controls, $n = 7$ patients with COVID-19 (E and F). Horizontal red lines indicate the medians. Mann-Whitney test (E and F); the P value is indicated when significant. Scale bars, 20 μm (A and B) or 10 μm (C and D).

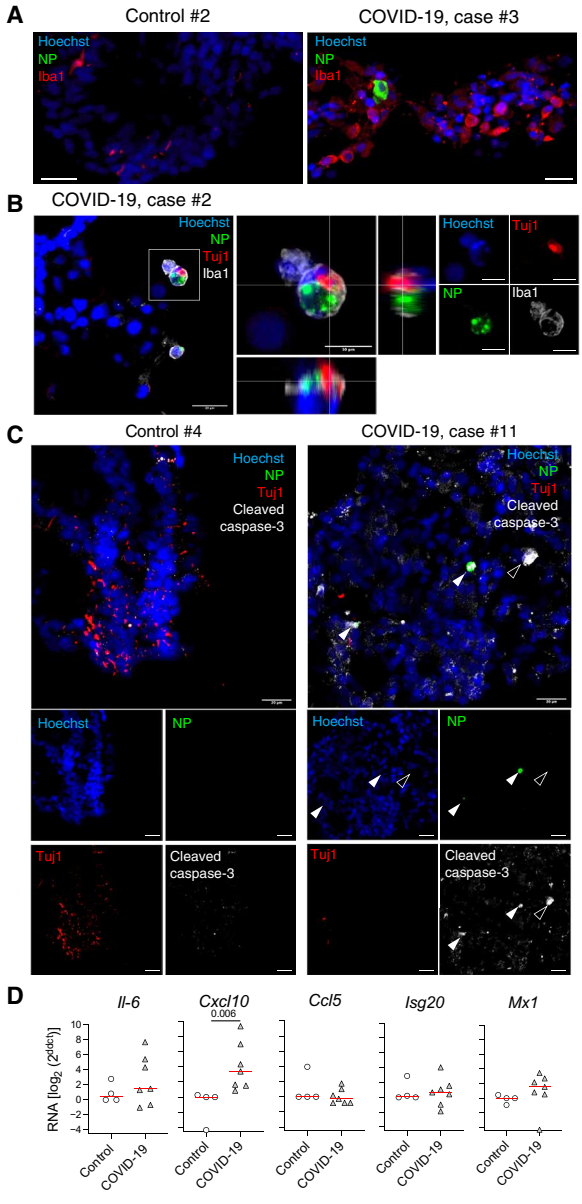

Fig. 2. Immune response in olfactory mucosa of patients with COVID-19 with acute olfactory function loss. (**A**) Immunofluorescence of myeloid cells (Iba1$^+$) retrieved from the olfactory mucosa of the control participant #2 versus case #3. (**B**) Orthogonal projection of Tuj1$^+$ antigens included in infected Iba1$^+$ cell. (**C**) Immunofluorescence of apoptotic cells (cleaved caspase-3$^+$) of control #4 and case #11. Solid arrowheads, infected cells positive for cleaved caspase-3. Empty arrowhead, noninfected cell positive for cleaved caspase-3. (**D**) Cytokines and chemokines transcripts in the olfactory mucosa. $n = 4$ controls, $n = 7$ patients with COVID-19. Horizontal red lines indicate the medians. Mann-Whitney test (D). The P value is indicated when significant. Scale bars, 20 or 10 μm (B, inset).

(Figs. 1E and 2A and tables S1 and S2). These data suggest that SARS-CoV-2 infection is associated with inflammation of the olfactory mucosa in patients with olfactory impairment; we thus measured the profile of local cytokine and inflammatory mediators. Expression of gene transcript of *Cxcl10* was elevated in the olfactory mucosa in most patients with detectable SARS-CoV-2 antigens as compared to control patients, and in contrast, an interindividual variability, both in SARS-CoV-2–infected and control individuals, was observed in *Il-6*, *Ccl5*, *Isg20*, and *Mx1* gene transcript expression (Fig. 2D and tables S1 and S2).

Together, this first set of data indicates that SARS-CoV-2 exhibits an unambiguous tropism for the olfactory neuroepithelium, and this infection is associated with increased local inflammation. We next investigated the identity of the cell types targeted by SARS-CoV-2. We detected SARS-CoV-2–infected mature sensory neurons (OMP$^+$; Fig. 1, B, C, and E, and tables S1 and S2); other SARS-CoV-2–infected cells were sustentacular cells (expressing CK18; Fig. 1, D and E, and fig. S1C) and myeloid cells (expressing Iba1; Figs. 1E and 2B and tables S1 and S2). We also detected the presence of immature sensory neurons (Tuj1$^+$) in the olfactory

mucosa of all patients, some of them being infected by SARS-CoV-2. Some Iba1- and SARS-CoV-2–positive cells were engulfing portions of Tuj1 cells in the olfactory mucosa of COVID case #2, suggesting that infected immature sensory neurons were in the process of being phagocytosed by innate immune cells (Fig. 2B). We next investigated whether infection induces cell death in the olfactory neuroepithelium, by cleaved caspase-3 staining. A strong cleaved caspase-3 signal was detected in both infected and noninfected cells in patients with COVID-19, whereas no signal was detected in samples from control individuals (Fig. 1, E and F; Fig. 2C; and tables S1 and S2). Together, these results show that a variety of cell types are infected in the olfactory neuroepithelium of patients with COVID-19, leading to increased cell death through apoptosis. Among them, the loss of mature OSNs might be critically relevant in the context of the anosmia. To further assess the impact of neuroepithelium infection by SARS-CoV-2, we infected Syrian golden hamsters to experimentally reproduce anosmia and ageusia and investigated the potential SARS-CoV-2 infection of the olfactory system and its upstream brain structures.

Modeling loss of taste and smell functions using SARS-CoV-2 nasal instillation in golden hamsters

Syrian golden hamsters (both sexes) were intranasally inoculated with 6×10^4 PFU of SARS-CoV-2 and followed up between 24 hours and 14 days post-inoculation (dpi). Clinical, sensorial, and behavioral functions were assessed at different time points (fig. S2A). SARS-CoV-2 inoculation resulted in a decrease in body weight and a degradation in the clinical score as early as 2 dpi, with a peak between 4 and 6 dpi, and sickness resolution by 14 dpi (Fig. 3, A and B). High viral loads were detected throughout the airways of infected hamsters at 2 and 4 dpi and remained detectable even at 14 dpi (Fig. 3C), consistent with the well-established respiratory tropism of SARS-CoV-2. In line with our observations in human samples, the nasal turbinates of infected hamsters exhibited high viral loads as soon as 2 dpi. Viral RNA was also detected from 2 dpi and onward in various parts of the brain, including the olfactory bulb, cerebral cortex, brain stem (diencephalon, midbrain, pons, and medulla oblongata), and cerebellum (Fig. 3D). In addition, we were able to isolate infectious viral particles from the nasal turbinates, the lung, and different brain areas (olfactory bulb, cerebral cortex, brain stem, and cerebellum), indicative of the replication and production of SARS-CoV-2 in the CNS of hamsters (Fig. 3E). Having shown the concomitant infection of nasal turbinates and the CNS, we further investigated their impact on sensory and behavioral responses.

We assessed both the gustatory and olfactory functions of SARS-CoV-2–inoculated hamsters. At 2 dpi, we subjected hamsters to a sucrose preference test. As expected, mock-infected animals displayed a clear preference toward sucrose-complemented water compared to control water, whereas infected hamsters had no preference toward the sucrose-complemented water (Fig. 4A), indicative of a SARS-CoV-2–associated dysgeusia/ageusia. Moreover, infected animals exhibited signs of hyposmia/anosmia during food finding experiments, because they needed more time to find hidden (buried) food than uninfected hamsters, and a substantial proportion of them (50% at 3 dpi and 37.5% at 5 dpi) failed to find the food at the end of the test (Fig. 4, B and C). Nevertheless, all infected hamsters succeeded to find visible food (Fig. 4C), revealing that no sickness behavior, visual impairment, or locomotor deficit accounted for the delay in finding the hidden food. In addition, no locomotor deficit was observed during either the open-field (fig. S2B) or painted footprint tests (fig. S2C), further excluding a motor deficit bias during the food finding test. At 14 dpi, when weight and clinical score had resumed to normal (Fig. 3, A and B), all hamsters successfully found the hidden food (Fig. 4C), indicating that infection-associated anosmia recovered spontaneously in this animal model.

SARS-CoV-2 promotes cellular damages in the olfactory epithelium of infected hamsters

We then investigated the impact of SARS-CoV-2 infection on hamster olfactory mucosa, which exhibited high viral loads (Fig. 3C). The uppermost part of nasal turbinates is overlaid by the olfactory neuroepithelium (Fig. 5A), a neuroepithelium composed of sensory neurons and supports sustentacular cells with both cell populations being ciliated. Imaging by scanning electron microscopy of the olfactory neuroepithelium showed an important loss of ciliation as early as 2 dpi (Fig. 5, B and C, and fig. S3) on large portions of the epithelial surface, indicating cilia loss in both OSNs and sustentacular cells. At 4 dpi, viral particles were seen budding from deciliated cells (Fig. 5D). At 14 dpi, the olfactory mucosa appeared ciliated anew, indistinguishable from that of mock-infected animals (Fig. 5E and fig. S3), consistent with the recovery of olfaction seen in infected hamsters (Fig. 4C).

In line with the detection of viral particles by electron microscopy at 4 dpi, SARS-CoV-2 was detected in the hamsters' olfactory mucosa at this time point, alongside an infiltration of myeloid $Iba1^+$ cells (Fig. 6, A to E and J). In the olfactory mucosa, SARS-CoV-2 antigens were found in the cytoplasm of mature (OMP^+; Fig. 6, A, B, and J) and immature ($Tuj1^+$; Fig. 6, C, D, and J) sensory neurons and in sustentacular cells ($CK18^+$; fig. S4, A and B). Some $Iba1^+$ immune cells seen infiltrating the neuroepithelium were positive for SARS-CoV-2, consistent with a potential secondary infection resulting from the phagocytosis of infected cells (Fig. 6D, arrow, and Fig. 6J). The areas of neuroepithelium containing infected cells were disorganized (see Fig. 6, B and D, and fig. S4B), whereas adjacent areas without SARS-CoV-2 remained morphologically intact (fig. S4C). Cilia of OMP^+ neurons located at the apical part of olfactory epithelium were lost in the disorganized infected neuroepithelium (Fig. 4B). As observed in human samples (see Fig. 2C), infection induced cell death, with many neuronal and non-neuronal cells being positive for cleaved caspase-3 in the olfactory mucosa of infected hamsters at 4 dpi (Fig. 6J and fig. S4D). We observed the expression of cleaved caspase-3 in infected and uninfected cells (fig. S4D), indicating that cell death is not only caused by cytopathic effects of SARS-CoV-2 but also probably caused by the local inflammation and immune responses to infection.

SARS-CoV-2 dissemination to the brain and neuroinflammation in infected hamsters

Having shown that SARS-CoV-2 infects OSNs and that SARS-CoV-2–infected hamsters exhibit signs of anosmia and ageusia, we wondered whether SARS-CoV-2 invades the CNS via a retrograde route from the olfactory system. SARS-CoV-2 was detected in olfactory nerve bundles close to the neuroepithelium, as demonstrated by the colocalization of SARS-CoV-2 NP antigen and OMP^+ sensory neuron axons reaching the olfactory bulb (Fig. 6, E, K, and L), consistent with a retrograde infection of axons. Furthermore, SARS-CoV-2 NP was detected at the junction of the olfactory nerve and olfactory

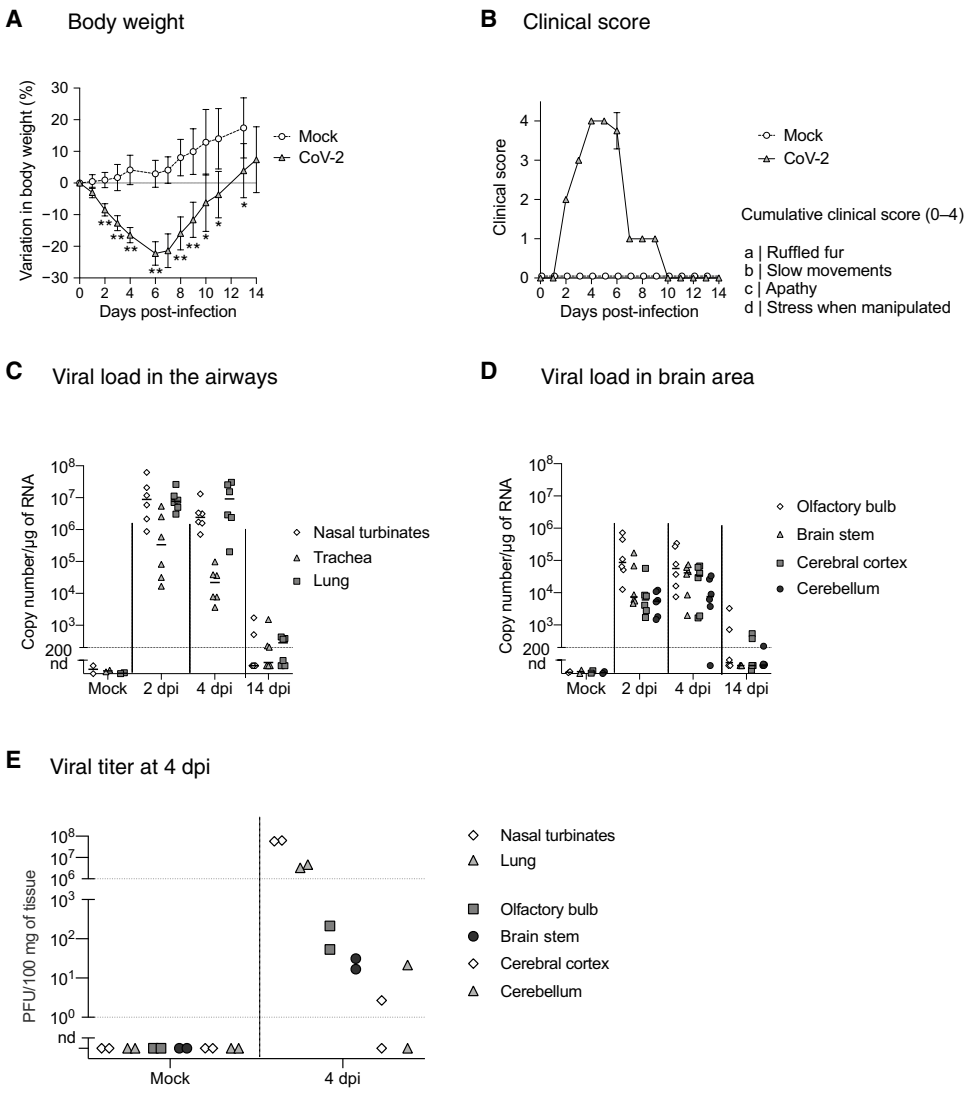

Fig. 3. Clinical and molecular characteristics of experimental infection with SARS-CoV-2 in golden hamsters. (**A** and **B**) Variation in body weight (A) and clinical score (B) of mock- and SARS-CoV-2–infected hamsters for 14 days post-inoculation (dpi). (**C** and **D**) Quantification of SARS-CoV-2 RNA in hamster airways (C) and in different brain areas (D) of mock and infected animals at 2, 4, and 14 dpi. (**E**) Infectious viral titer in the nasal turbinates, lung, olfactory bulb, brain stem, cerebral cortex, and cerebellum at 4 dpi expressed as plaque-forming units (PFU)/100 mg of tissue. Horizontal lines indicate medians. $n = 4$ to 8 per time point in (A) and (B); $n = 6$ per time point in (C) and (D); $n = 2$ per time point in (E). Mann-Whitney test comparing infected animals to mock (A). $^{*}P < 0.05$; $^{**}P < 0.01$. nd, no detection.

bulb, seemingly infecting cells of neuronal/glial morphology (Fig. 6F). In the olfactory bulb, SARS-CoV-2 NP was detected in Iba1^{+} cells (Fig. 6H) and in uncharacterized cells (Fig. 6, I and L) in the glomerular layer of the olfactory bulb. The viral NP was not detected in other areas of the brain. The high viral RNA loads in the nasal turbinates and in the olfactory bulb, together with the observation of viral antigens along the entire route from the olfactory sensory organ to the bulb, suggest that SARS-CoV-2 enters the brain through the olfactory system, although this finding does not rule out other ports of CNS entry in patients with COVID-19.

In the nasal turbinates, we detected an intense proinflammatory environment, with an up-regulation of *Il-6*, *Cxcl10*, *Ifn*-β, *Ifn*-λ, and *Il-1*β at 2 dpi and a slight decrease at 4 and 14 dpi (Fig. 6M). Similarly, the olfactory bulb exhibited an important up-regulation in the expression of these genes (Fig. 6N), but in a different and delayed pattern compared to the nasal turbinates: Whereas *Cxcl10* was overexpressed throughout the infection, there was no change in *Ifn*-λ gene expression, and the increase in *Il-6*, *Ifn*-β, and *Il-1*β gene transcripts was observed only from 4 dpi, with *Il-1*β remaining up-regulated up to 14 dpi. These data reveal bulbar inflammation during the SARS-CoV-2 infection, possibly in response to signaling via olfactory nerves.

Using RNA sequencing (RNA-seq), we observed 374 and 51 differentially expressed genes (DEGs; increased or decreased, respectively) in the olfactory bulbs of SARS-CoV-2–infected hamsters at 4 dpi (Fig. 7A). The DEGs were classified according to KEGG (Kyoto Encyclopedia of Genes and Genomes) pathways (Fig. 7B) and the GO (gene ontology) terms on the basis of their biological processes, molecular functions, and cellular components (Fig. 7C). Up-regulated genes were mainly involved in inflammatory responses and responses to virus infection, with innate immunity components [type I interferon (IFN)–mediated response, natural killer cell activation, Toll-like receptors, retinoic acid–inducible gene-1–like receptors, nuclear factor κB, and Janus kinase–signal transducers and activators of transcription (Jak-STAT) signaling pathways], adaptive immunity components [T helper cell 1 (T_H1), T_H2, and CD4^{+} T cells], and functions related to chemokine signaling. Other biological processes related to nervous system functions were synapse pruning, up-regulation of the neuroinflammatory response, and both astrocyte and microglial activation. To validate the involvement of these signaling pathways, we analyzed the expression of selected targets in the olfactory bulb by RT-qPCR (Fig. 7D). The genes *Mx2*, *Irf7*, *Ddx58*, and *Stat1* were found up-regulated early in the infection (2 and 4 dpi), whereas *Ccl5* was up-regulated only at 4 dpi. The overexpression of *Ccl5* and *Irf7* persisted even at 14 dpi. Together, SARS-CoV-2–associated inflammation in the bulb confirmed by unbiased RNA-seq analysis, along with the increased viral load detected in the brain parenchyma, supports the assumption that SARS-CoV-2 neuroinvasion drives the neuroinflammation. *Cxcl10*, *Il-1*β, *Ccl5*, and *Irf7* overexpression persisted up to 14 dpi, when animals had recovered from ageusia/anosmia. These data indicate that an infectious or postinfectious inflammatory process persists even in the asymptomatic or in a delayed post-symptomatic phase in our animal model.

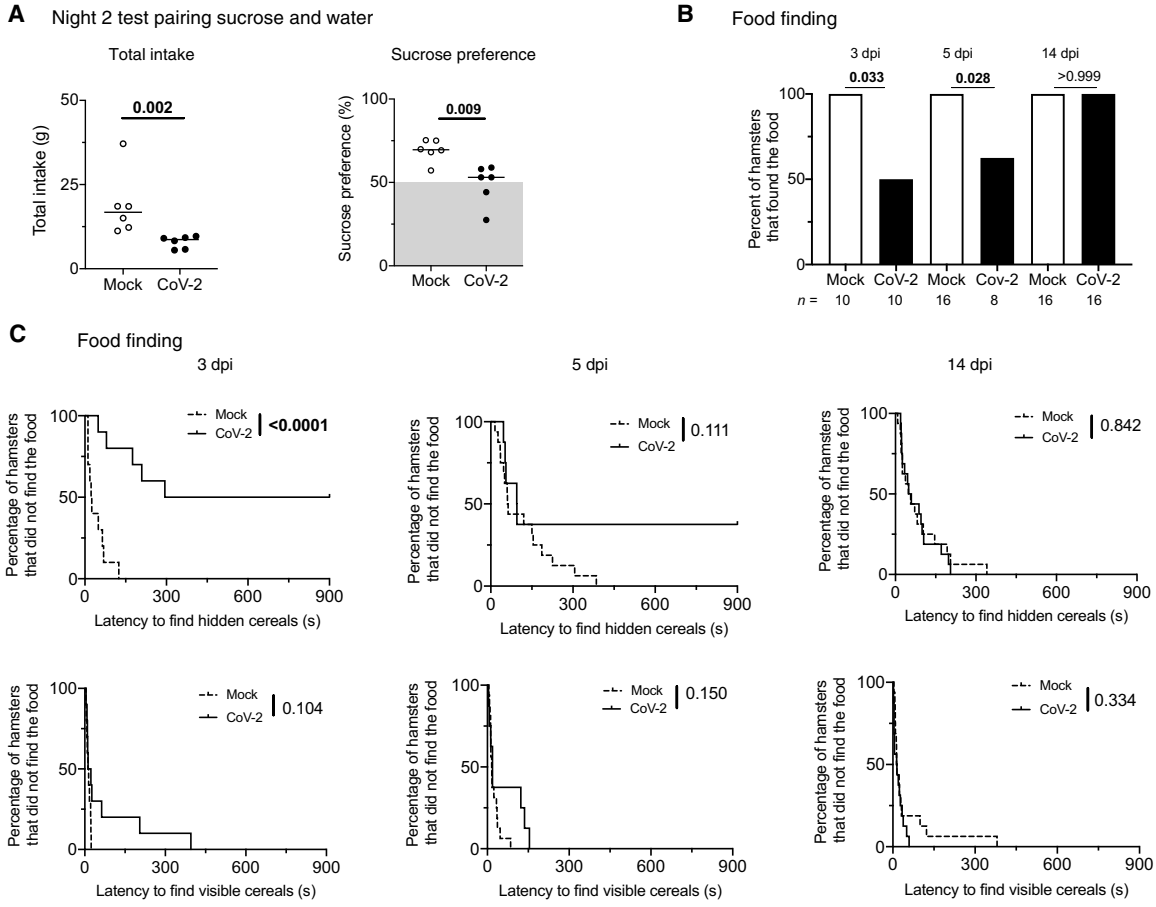

Fig. 4. Experimental infection with SARS-CoV-2 in golden hamster induces transient anosmia and ageusia. (**A**) Variation in total consumption of liquid overnight and preference toward 2% sucrose-containing water of control and SARS-CoV-2–infected hamsters at 2 dpi. (**B**) Fraction of control or infected hamsters successfully finding hidden food in 15 min. (**C**) Fraction of control or infected hamsters successfully finding hidden or visible food over time. Food-finding assays were performed at 3, 5, and 14 dpi. Mann-Whitney test (A), Fisher's exact test (B), and log-rank (Matel-Cox) test (C). *P* value is indicated in bold when significant. Bars indicate medians. $n = 6$ per group in (A); $n = 10$ mock and $n = 10$ CoV-2 at 3 dpi, $n = 16$ mock and $n = 8$ CoV-2 at 5 dpi, $n = 16$ per group at 14 dpi in (B) and (C).

SARS-CoV-2 persistence in human olfactory mucosa with long-lasting/relapsing loss of smell

In some patients, neurological impairments and/or sensory dysfunctions persist several months later from the onset of COVID-19 symptoms, and it has been proposed that this may be linked to persistent viral infection and/or inflammation (*31*, *32*). We recruited four patients with prolonged/recurrent olfactory function loss after COVID-19. The main characteristics of these patients are listed in table S4. They were recruited between 15 and 29 July 2020, at a time when viral circulation in Paris was very low (<10 cases per 100,000 inhabitants/week), implying that SARS-CoV-2 reinfection of these patients was very unlikely. In these cases, the time from first COVID-19–related symptoms to inclusion ranged from 110 to 196 days. As a control, we sought to include patients with confirmed COVID-19 but without loss of smell. However, given the relative invasiveness of the olfactory epithelium brushing, the sampling of SARS-CoV-2–infected patients with neither loss of smell nor ENT care was not possible, except for a single individual (47-year-old man, recruited in July 2020) presenting long-lasting COVID-19 symptoms (such as dysgeusia, vertigo, paresthesia and tremor, and tingling of the face, nose, arms, and legs, persisting for >141 days) but without any history of anosmia (table S4).

The four patients with long-lasting/relapsing loss of smell had been diagnosed with COVID-19 between January and March 2020 on the basis of their initial clinical assessment, including sudden anosmia at disease onset, accompanied with taste changes (except case #8) and at least one clinical sign related to COVID-19, such as not only fever, fatigue, diarrhea, cough, dyspnea, headache, muscle pain, laryngitis, and sore throat but also paresthesia and vertigo in some patients (Fig. 8A). Smell loss was complete at disease onset for these patients. Other otolaryngologic symptoms were rhinorrhea for two patients, not concomitant with smell loss and nasal irritation for three patients. Nasal obstruction was reported in patient #10. All had persistent smell loss, persistent taste dysfunction (except case #8), and/or other neurological deficits after COVID-19 at inclusion (Fig. 8A) and were seen at the ENT department for this reason. Neurological signs were stereotypical crises of wriggling nose, left intercostal and nonspecific arm pain (case #8), paresthesia (case #9), and vertigo (case #10). The characteristics of taste and smell abnormalities at inclusion are described in table S5. Two patients complained of bad taste (table S2). Reduced or increased acuity for bitter and reduced acuity for salt or sour were reported by the two patients with dysgeusia. None of the patients required hospitalization.

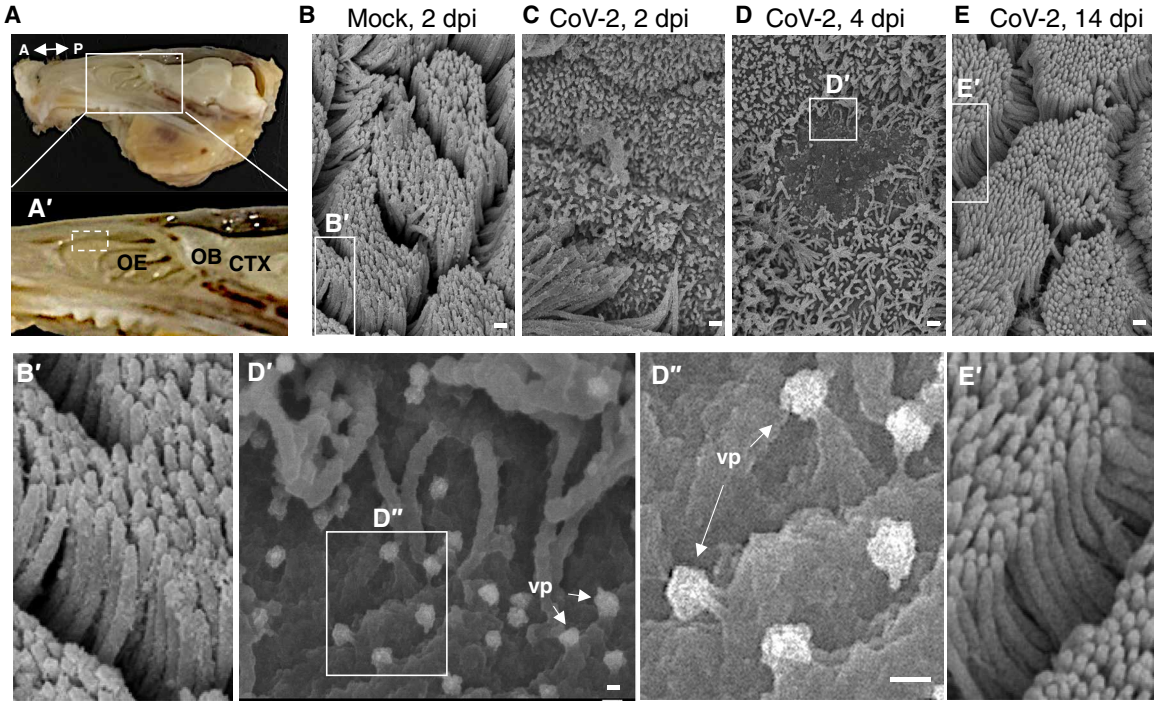

Fig. 5. SARS-CoV-2 induces loss of ciliation in the olfactory epithelium. (**A**) Dissected hamster head, skin, and lower jaw were removed, sagitally cut in half. Double-headed arrow denotes the anteroposterior (A-P) axis. Close-up in (A′) shows the close relationship between the olfactory epithelium (OE), the olfactory bulb (OB), and the cerebral cortex (CTX). Discontinuous square indicates the area collected for scanning electron microscopy. (**B** to **E**) Scanning electron microscope imaging showing changes in olfactory epithelium after SARS-CoV-2 infection. The olfactory epithelium of mock-infected (B and B′) and CoV-2–inoculated hamsters at 2 dpi (C), 4 dpi (D, D′, and D″), and 14 dpi (E and E′). A loss of cilia is observed at 2 and 4 dpi for infected hamsters. Viral particles (vp) are seen emerging from deciliated cells (D′ and D″, white arrows). Scale bars, 1 μm (B to E) and 100 nm (D′ and D″).

These four patients, when consulting with long-lasting/relapsing loss of smell, had no detectable SARS-CoV-2 RNA in nasopharyngeal samples by means of routine diagnosis RT-qPCR. However, all of them had detectable SARS-CoV-2 RNA in cytological samples from the olfactory mucosa, using the RT-qPCR SYBR technique (table S4). Furthermore, three of them (#8, #9, and #10) had a high viral genomic RNA load in the olfactory mucosa (1.68×10^5 to 4.35×10^5 RNA copies/μl; TaqMan technique), but no subgenomic RNA was detected (table S4), in favor of a lack of active SARS-CoV-2 replication in the analyzed samples. We further evaluated olfactory mucosa infection by immunofluorescence labeling. We found variable cellularity between olfactory mucosa samples within patients, but all samples contained OSNs, positive for Tuj1, indicating the efficient sampling of the neuroepithelium. Immunostaining revealed the presence of SARS-CoV-2 antigens (N protein) in three of four patients (table S4 and Fig. 8, B and D). We observed abundant $Iba1^+$ immune cells in the olfactory mucosa of all four patients (table S4 and Fig. 8, B, D, and E), and apoptotic cells (cleaved caspase-3 positive) were observed in the samples of all these patients (Fig. 8, D and E, and table S4). Quantification of *IL-6* gene expression revealed an up-regulation of this proinflammatory cytokine in the olfactory mucosa of the three patients with high viral load, but not in case #6, which nevertheless presented SARS-CoV-2 antigens in the neuroepithelium (table S4). *IL-6* expression in patients with persistent signs of COVID-19 was similar to those of patients with acute COVID-19 (tables S1 and S2 and Fig. 8C). No changes were observed in *Ccl5*, *Cxcl10*, *Isg20*, and *Mx1* transcripts (table S4).

Patient #7, exhibiting long-lasting COVID-19 symptoms but normal sense of smell, had no detectable SARS-CoV-2 RNA in nasopharyngeal samples at inclusion. However, this patient had detectable SARS-CoV-2 RNA in the nasal cytobrush sample using the RT-qPCR SYBR technique and a quantifiable viral genomic RNA load (1.88×10^5 RNA copies/μl; TaqMan technique), but neither subgenomic RNA nor SARS-CoV-2 antigen (NP protein) was detected in the olfactory mucosa by immunostaining (Fig. 8D and table S4). Having found that a prolonged carriage of SARS-CoV-2 in the olfactory mucosa is not necessarily associated with loss of smell, we investigated immune responses in the olfactory neuroepithelium of this patient. Although *IL-6* expression was high in this patient's sample, very few myeloid cells ($Iba1^+$) were observed, and no cell death was detected in harvested cells (Fig. 8E and table S4).

Together, these data indicate that the olfactory neuroepithelium from patients with persistent loss of smell remains infected, with continual SARS-CoV-2 RNA in all of them and persevering inflammation. Because sustained infection was also found in a patient with long-lasting COVID-19 symptoms and normal sense of smell, but with seemingly less severe inflammation of the olfactory mucosa, we hypothesize that persistence of COVID-19–associated loss of smell is linked to the inflammation caused by persistent infection.

DISCUSSION

By combining investigations of COVID-19–associated olfactory function loss in patients and experimentally infected hamsters, both

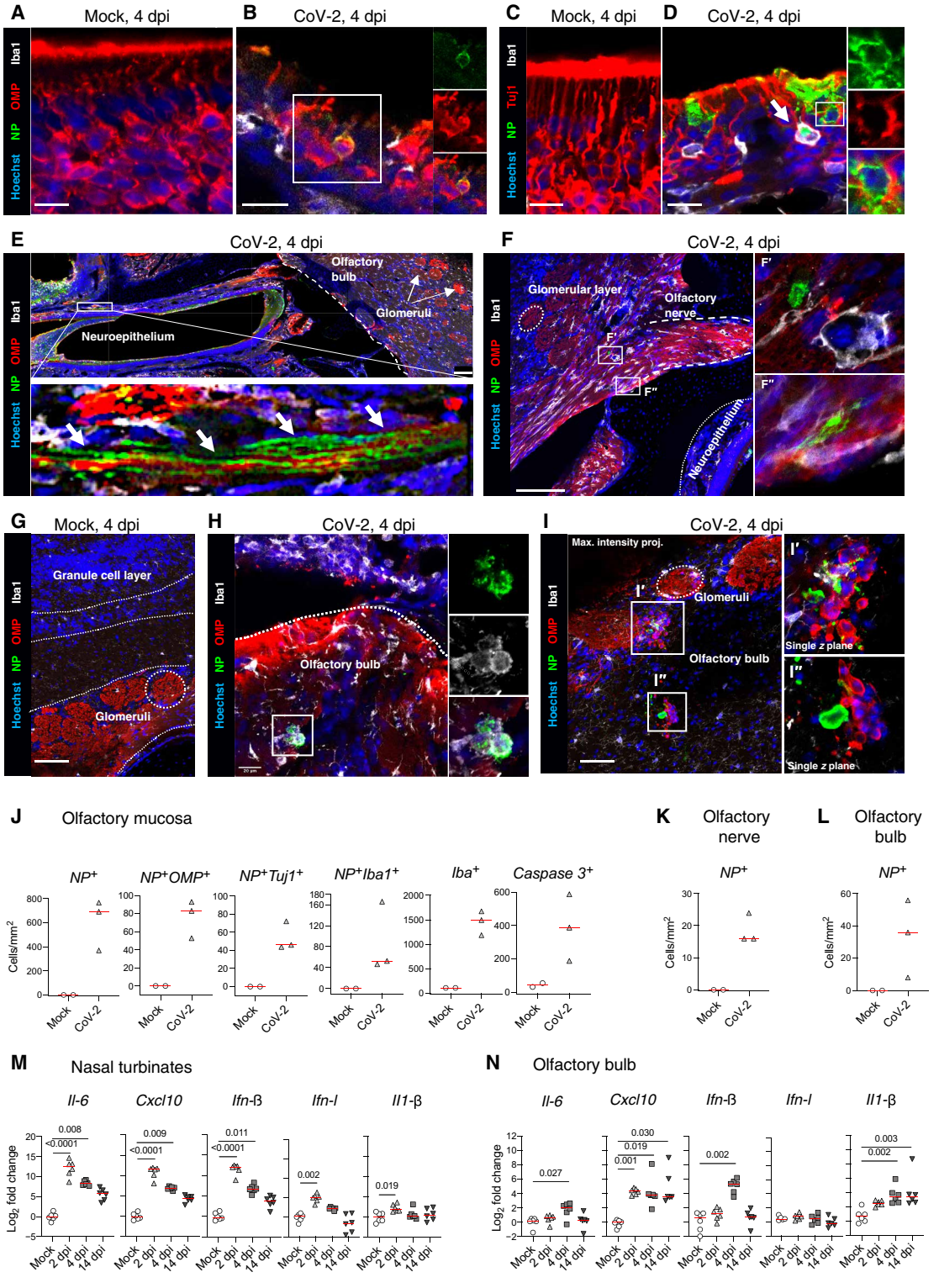

Fig. 6. SARS-CoV-2 antigen detection and cytokine/chemokine transcript quantification in the olfactory system of hamsters. (**A** to **D**) Olfactory epithelium of mock-infected (A and C) and SARS-CoV-2–infected (B and D) hamsters at 4 dpi. Insets show infected OMP$^+$ mature OSNs (B) or infected Tuj1$^+$ immature OSNs (D). The arrow in (D) indicates an infected Iba1$^+$ cell. (**E**) Sagittal section showing nasal turbinates and olfactory bulb of SARS-CoV-2–infected hamster at 4 dpi. Inset depicts SARS-CoV-2 staining in OSN axons. (**F**) Olfactory sensory axons projecting into glomeruli in the olfactory bulb of SARS-CoV-2–inoculated hamsters at 4 dpi. Insets (F′ and F″) show infected cells. (**G** to **I**) Olfactory bulb of mock-infected (G) or SARS-CoV-2–infected (H and I) hamsters at 4 dpi. Iba1$^+$ infected cells are shown in (H), and several infected cells are observed in (I). SARS-CoV-2 is detected by antibodies raised against the viral NP. Scale bars, 20 μm (A to D and H), 100 μm (E and F), and 50 μm (G and I). Images are single *z* planes (A to H) or maximum intensity projection over a 6-μm depth (I). (**J**) Number of NP$^+$ cells, NP$^+$OMP$^+$ cells, NP$^+$Tuj1$^+$ cells, NP$^+$Iba1$^+$, Iba1$^+$ cells, and cleaved caspase-3$^+$ cells in the olfactory mucosa. (**K** and **L**) Number of NP$^+$ cells in the olfactory nerve (K) and the olfactory bulb (L). (**M** and **N**) Cytokines and chemokines transcripts in the nasal turbinates (M) and in the olfactory bulb (N) at 2, 4, and 14 dpi. Kruskal-Wallis followed by the Dunn's multiple comparison test (M and N). The *P* value is indicated when significant. Horizontal red lines indicate the medians.

naturally permissive to SARS-CoV-2 infection, we demonstrate that multiple cell types of the olfactory neuroepithelium are infected during the acute phase, at the time when loss of smell manifests. Protracted viral infection and inflammation in the olfactory neuroepithelium may account for prolonged hyposmia/anosmia. Olfactory mucosa cytological sampling collected from acute or chronic patients with COVID-19 with olfactory function loss revealed the presence of the SARS-CoV-2 in 100% of patients (n = 11), whereas the virus was undetected by RT-qPCR performed at inclusion on conventional nasopharyngeal swabs. Therefore, diagnosing

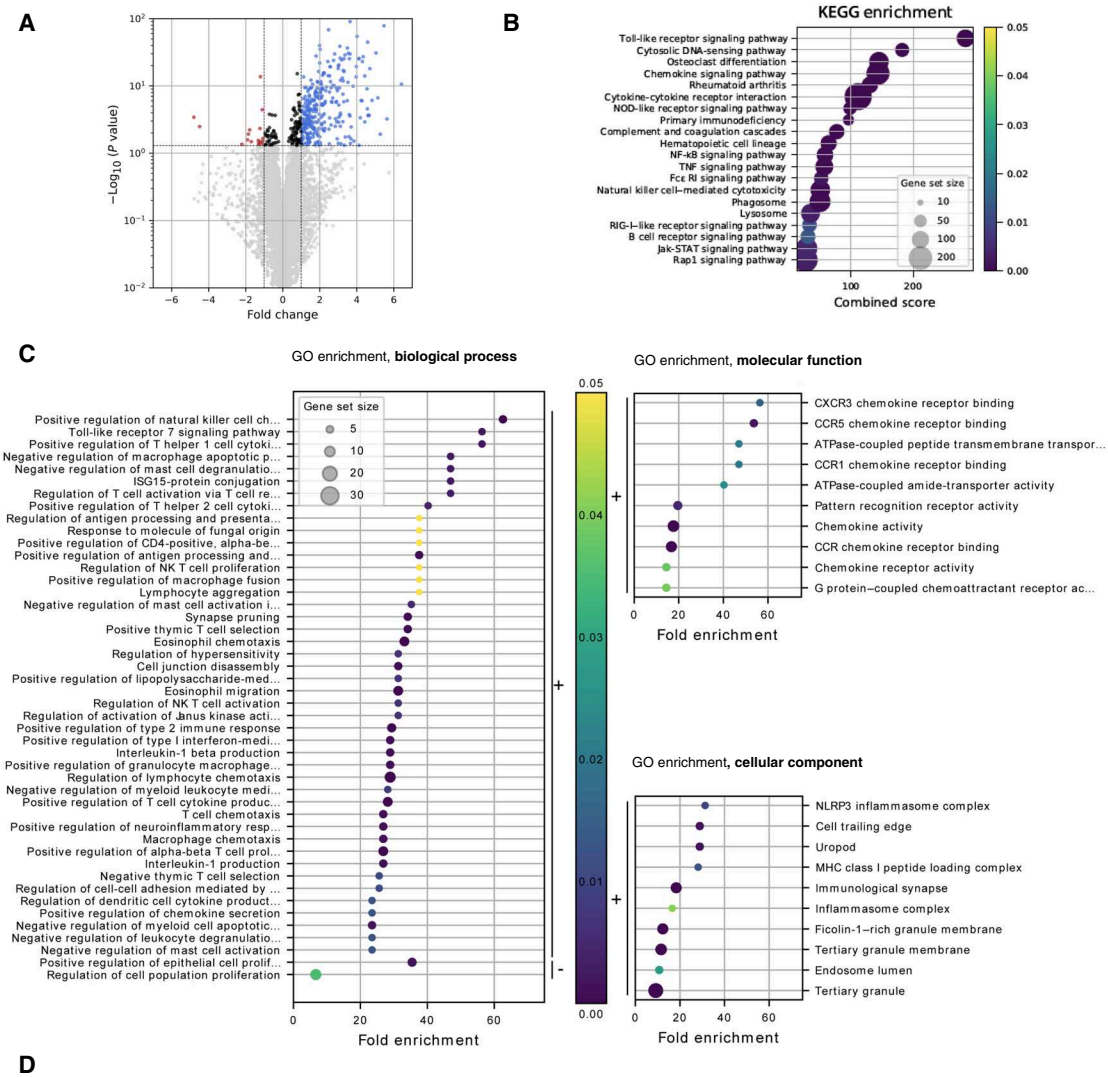

Fig. 7. DEGs in the olfactory bulb of golden hamsters infected by SARS-CoV-2 (at 4 dpi) derived by RNA-seq. (**A**). Volcano plot of the comparisons between infected and noninfected samples. *Y* axis represents the Benjamini-Hochberg–corrected *P* value on a logarithmic scale ($-\log_{10}$). Gray dots represent genes not passing a threshold of false discovery rate (FDR) < 0.05. Black dots represent genes passing the FDR threshold but having fold changes between −1 and 1. Red and blue dots correspond to significant down- and up-regulated genes with a fold change inferior to −1 or superior to 1, respectively. (**B**). KEGG pathways enrichment based on the differentially regulated genes between infected and noninfected samples. Only the 20 highest combined scores are plotted. Circle sizes are proportional to the gene set size. Circle color is proportional to the corrected *P* values and corresponds to the scale presented in (C) and (D). ISG15, interferon-stimulated gene 15; NOD, nucleotide-binding oligomerization domain; NF-κB, nuclear factor κB; TNF, tumor necrosis factor; RIG-1, retinoic acid–inducible gene-1. (**C**) GO enrichment analysis considering biological process only. Selected GO terms are based on the up- and down-regulated genes between infected and noninfected samples. The black bars on the right-hand side of the scatterplot indicate enrichment based on down-regulated ("−") and up-regulated ("+") gene sets. Only the 50 highest fold enrichments are plotted for the up-regulated gene set. Circle sizes are proportional to the gene set size, which shows the total size of the gene set associated with GO terms. Circle color is proportional to the corrected *P* values and corresponds to the scale presented between (C) and (D) GO enrichment analysis, considering molecular function– and cellular components–related figures follow the same construction as in biological process, with the exception that only the 10 highest fold enrichments are plotted for the up-regulated gene set. NK, natural killer; ATPase adenosine triphosphatase; MHC, majos histocompatibility complex. (**D**) Validation targets in the olfactory bulb at 2, 4, and 14 dpi. $n = 6$ per time point. The *P* value is indicated when significant. Horizontal lines indicate the medians. Complete analysis is listed in data file S2.

SARS-CoV-2 infection in olfactory mucosa sampled by use of nasal cytobrushes is a more sensitive approach, at least in patients with olfactory function loss, than conventional nasopharyngeal samples. This presence of SARS-CoV-2 RNA and proteins may influence care management of patients with COVID-19 because it may play a role in virus transmission from patients who are thought to be viral free on the basis of conventional testing, particularly in individuals with mild or no symptoms.

We therefore confirm that SARS-CoV-2 has a tropism for the olfactory mucosa (*33*), and we demonstrate that it can persist locally,

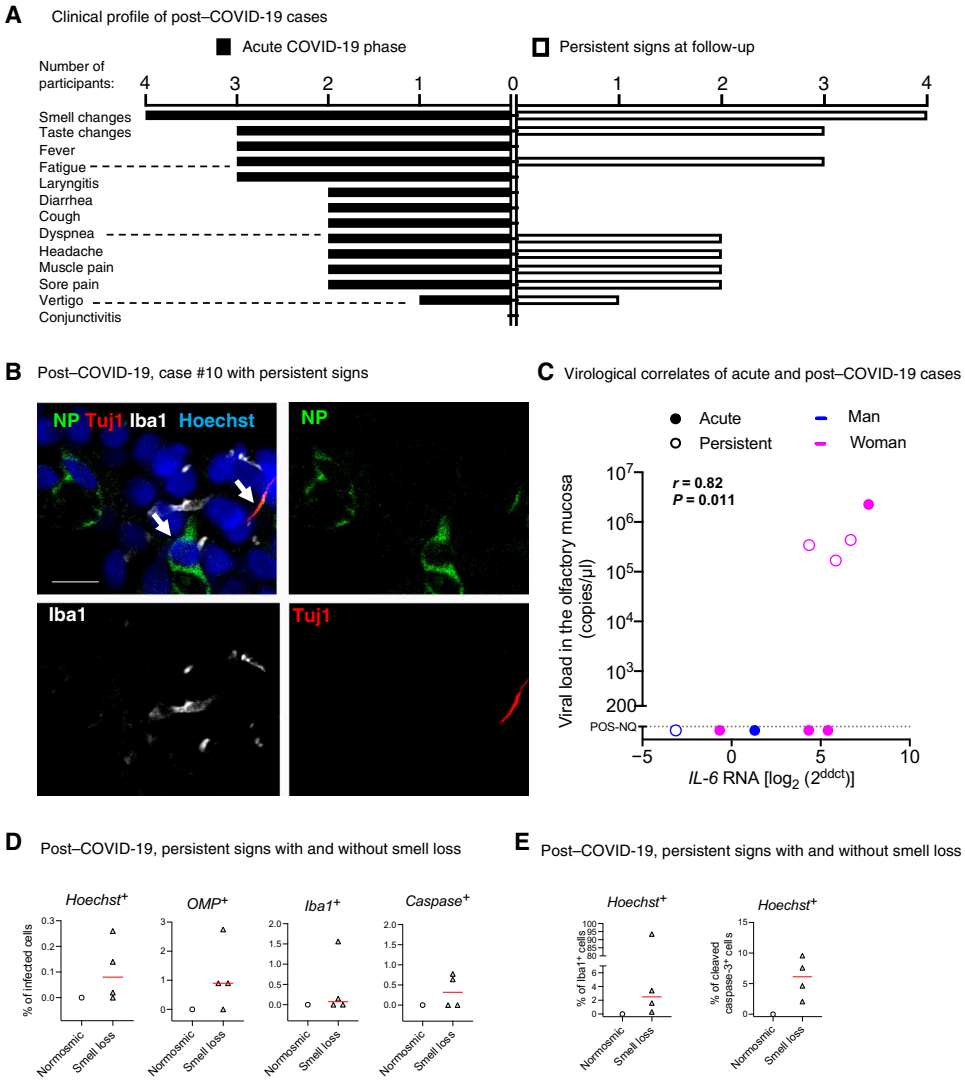

Fig. 8. SARS-CoV-2 is present in the olfactory mucosa from patients with persistent loss of smell post–COVID-19. (**A**) Clinical profile of the four patients with prolonged loss of smell post–COVID-19. The general symptoms at the acute phase and at the follow-up (inclusion in CovidSmell study) are shown. (**B**) Immunofluorescence of infected cells in the olfactory mucosa of case #10 presenting with persistent olfactory dysfunction at 196 days after COVID-19 onset. The left arrow indicates an infected cell with viral NP staining. The right arrow indicates a Tuj1-NP colabeling in another cell. (**C**) Graph depicting the correlation between the *IL-6* mRNA expression and the viral load in the nine patients with acute COVID-19 ("acute," $n = 5$) or persistent olfactory dysfunction post–COVID-19 ("persistent," $n = 4$). (**D** and **E**) Fraction of infected cells among the following: Hoechst$^+$ cells, OMP$^+$ cells, Iba1$^+$ cells, and cleaved caspase-3$^+$ cells (D), and fraction of Iba1$^+$ cells among Hoechst$^+$ cells (E, left) and fraction of cleaved caspase-3$^+$ cells among Hoechst$^+$ cells (E, right) in the olfactory mucosa of patients with persistent loss of smell post–COVID-19 ($n = 4$) and the patient #7 (post–COVID-19, persistent signs without loss of smell). Viral load values were assessed by TaqMan qPCR; when not quantifiable (nq) (<200 copies/µl), they were arbitrarily given the 50 value for Spearman test (C). Variations in the cytokine gene expression were calculated as the *n*-fold change in expression in the swabs compared with the swab value of control #1 that was arbitrarily put on zero value. Horizontal red lines indicate the medians (D and E). Mann-Whitney test (D and E) and Spearman test (C). Scale bar, 10 µm.

not only a few weeks after general symptoms resolution (*34*–*36*) but also several months in OSNs. Hence, we found that SARS-CoV-2 persists in the olfactory mucosa of patients with prolonged olfactory function loss, up to 6 months after initial diagnosis. Sampling of the olfactory mucosa revealed viral RNA and viral antigens, indicating that long-lasting olfactory function loss in these patients correlates with persistence of both viral infection and inflammation, as shown by high expression of inflammatory cytokines including interleukin-6 (IL-6) and the presence of myeloid cells in cytological samples. Although reinfection by SARS-CoV-2 could not be formally excluded in these patients (*31*), the fact that they showed uninterrupted olfactory dysfunction since the onset of the disease, as well as the very low incidence of COVID-19 in France at the time of inclusion, does not support this option. However, there is no absolute correlation between long-term virus carriage and clinical signs, as we also reported here one long COVID-19 case presenting with persistent viral infection without concomitant loss of smell (but with concomitant dysgeusia). The most likely explanation to this observation is the variability of inflammation associated to long-term SARS-CoV-2 carriage, which can be fully asymptomatic (*37*, *38*) or associated with local inflammation and symptoms, such as in the patients who participated in this study. In addition, in the single patient with COVID-19 but without loss of smell, no cell death or immune cells were observed in the olfactory mucosa, but IL-6 was elevated. Therefore, it will be important to formally evaluate the extent of acute inflammation, immune cell infiltration, and cell and tissue damages among larger cohorts of patients with varying degrees of smell loss to extend our observations made on human olfactory mucosa and to identify the most important determinants of anosmia.

To further study anosmia and the inflammatory process in the olfactory system in the context of COVID-19, we used the golden hamster as an animal model for COVID-19. We show that intranasal SARS-CoV-2 inoculation in hamsters leads to infection of OSNs and induces anosmia, accurately recapitulating what is observed in patients, both clinically and histopathologically. Infection of OSNs in SARS-CoV-2–inoculated hamsters has been reported in experiments using similar viral inoculum (*26*), but not when the inoculum was lower (*27*), suggesting a dose-dependent susceptibility of OSNs to infection (*5*, *27*, *39*, *40*). Olfactory neurons express neuropilin-1, a membrane protein involved in SARS-CoV-2 cell entry (*5*), which may account for olfactory neuron infection. However, they almost do not express SARS-CoV-2 primary receptor ACE2 (*41*), as opposed to sustentacular cells. Infection of OSNs may happen after infection

of adjacent sustentacular cells and horizontally spread of the virus to a neighboring cell. Furthermore, the infiltration of immune cells and the disruption of tissue architecture may contribute to the dissemination of the virus across cells in the olfactory epithelium.

As observed in the tracheal epithelium (*42*), infection of the neuroepithelium is associated with cilia loss of the OSNs. Once cilia are restored in the late phase of infection (14 dpi in hamsters), olfaction resumes. Given that odorant receptors accumulate on sensory cilia in the olfactory epithelium, loss of smell in COVID-19 may be explained by the viral-induced cell death of olfactory neurons, or/and also by the disruption of their ciliary structure, preventing the detection of odorant molecules. Although not mutually exclusive, the latter hypothesis would explain why during COVID-19, the onset of anosmia is very sudden, before any other respiratory symptoms. Overall, anosmia likely reflects an infection-associated sensorineural dysfunction, which might involve a substantial inflammatory process, neuronal infection, deciliation, and cell death, rather than a simple nostril obstruction or tissue edema. The molecular mechanisms underlying neuronal dysfunction remain to be deciphered, but we recently reported that ivermectin strongly reduces loss of smell and is associated to a decrease in inflammation in the nasal turbinates of infected hamsters, without decreasing viral load (*43*). Therefore, immune responses induced by olfactory neuron infection might play a role in the onset and persistence of anosmia and could explain why some infected individuals with SARS-CoV-2 in their nasal cavity never develop anosmia.

We also found that this inflammatory process that takes place in the nasal cavity spreads to the olfactory bulb. This inflammatory transcriptional signature, as shown by RNA-seq and confirmed by qPCR for *Il-6*, type I IFN (*Ifn*-β), and *Cxcl10*, is consistent with the recent neuropathological description of deceased patients with COVID-19, where microgliosis was seen in the olfactory bulb (*12*). The fact that similar neuropathological alterations are observed in patients with COVID-19 and infected hamsters implies that these lesions are likely caused by SARS-CoV-2 infection, rather than a consequence of intensive care provided to patients with COVID-19, as previously hypothesized (*44*).

Although several viruses are known to invade and disseminate into the brain, whether SARS-CoV-2 does so is highly debated. For instance, viral RNA has been detected in the cerebrospinal fluid and other brain tissues collected from patients who died from COVID-19 (*12*), but the neuropathological relevance of these observations remains unclear (*6*, *13*, *45*). The potential SARS-CoV-2 portals of entry to the CNS are (i) retrograde neuroinvasion (via OSNs, glossopharyngeal nerve, and/or vagal nerve), (ii) via the blood-brain barrier endothelium (*13*, *46*), and (iii) via peripheral immune cells infiltration (such as T cells or peripheral macrophages). Although this does not rule out other routes, our study indicates that SARS-CoV-2 indeed does invade the CNS via the retrograde olfactory pathway. In addition to the olfactory bulb, viable SARS-CoV-2 was also detected in more remote brain areas of infected hamsters, such as the cerebral cortex and the brain stem, yet without clear visualization of viral antigens. Similarly, viral RNA or protein was observed in the brain stem of patients with COVID-19 (*12*, *39*), the location of central cardiorespiratory nuclei. Infection of these areas might contribute to the pathogenesis of the respiratory distress reported in patients with COVID-19, and this study therefore constitutes an important step toward elucidating COVID-19–associated putative neurological dysfunctions. Whether neuronal structures are directly targeted by SARS-CoV-2, as opposed to damaged by systemic immune responses, is of particular clinical relevance because these two scenarios would require different therapeutic strategies.

Limitations of our study includes the small sample size of the human cohort, especially for patients with COVID-19 without loss of smell. Extending these investigations to a larger group of patients, with varying degree of loss of smell, would allow to precise these first findings. Moreover, this study would benefit from additional approaches to determine the potential dysfunction of brain structures such as the olfactory bulb, by using metabolic positron emission tomography scan imaging as well as in-depth neurosensory and neurocognitive assessment. Last, the discovered persistence of SARS-CoV-2 in the olfactory mucosa of patients with long-lasting COVID-19 symptoms requires future validation in larger groups of people from different countries and to set up new animal models of long COVID.

The persistence of long-lasting COVID-19 symptoms is an important and topical issue as the pandemic continues (*47*). This study demonstrates a persistent loss of olfactory function in humans with SARS-CoV-2, for multiple months, lasting as long as the virus remains in the same microenvironment. This might result from direct damage to the OSNs, which detect odor in the olfactory epithelium. Further, it provides evidence of SARS-CoV-2 retrograde neuroinvasion via the olfactory route leading to neuroinflammation and shows the association between viral presence in the olfactory epithelium and anosmia, in both acute cases (hamsters and humans) and long-lasting cases (patients with COVID-19). The findings that we obtained are clinically relevant in the care to patients with COVID-19, because olfactory function loss could be regarded as a sensitive sign of persistent viral infection, and should be considered in patient management.

MATERIALS AND METHODS

Study design

The main objective of this study was to investigate SARS-CoV-2 neuroinvasion in humans and the hamster model and to decipher the molecular mechanisms involved. Human olfactory mucosa samples were obtained from a total of 16 living individuals (12 patients with COVID-19 and 4 healthy controls) at the ENT Department of Lariboisière Hospital, Paris, France, from May to October 2020. All these individuals were recruited in the CovidSmell study (Study of the Pathogenesis of Olfactory Disorders in COVID-19, ClinicalTrials.gov identifier NCT 04366934). This prospective, case-control study is a nontrial, nondrug study, qualified as exploratory, descriptive, monocentric, in an adult population. This study received the approval from the ethical committee "Comité de Protection des Personnes SUD EST IV" under reference 20.04.15.64936 and is compliant with French data protection regulations. All animal experiments were performed according to the French legislation and in compliance with the European Communities Council Directives (2010/63/UE, French Law 2013–118, 6 February 2013). The Animal Experimentation Ethics Committee (CETEA 89) of the Institut Pasteur approved this study (200023; APAFIS#25326-2020050617114340 v2.) before experiments were initiated. All animals were randomized to the different experimental groups. Sample sizes were chosen empirically to ensure adequate statistical power. Investigators were not blinded with respect to the origin of the samples. For analysis of the

human mucosa, two nasal samples were collected for each participant (one sample per nostril; one immediately frozen and the other one fixed in formalin). Each nasal sample was analyzed three times for SARS-CoV-2 assay by PCR (frozen samples) and immunohistochemistry (formol samples). Nasal samples of two patients and two controls were also titrated for SARS-CoV-2 on cell cultures. In animal experiments, at least four males were used for each time point, and replication was performed with the same number of females. Animal samples were analyzed three times for SARS-CoV-2 assay by PCR (frozen samples), immunohistochemistry (formol samples), and titrated by cell cultures (frozen samples). Olfactory mucosa samples of two controls and five SARS-CoV-2–infected hamsters were analyzed for SARS-CoV-2 by scanning electron microscopy and two controls and three infected hamsters for immunofluorescence. For microscopy quantification, the value for each animal is the average of four to eight independently quantified fields. All measurements in humans and hamsters were included in our analysis. Primary data are provided in the figures or the Supplementary Materials.

Participants

Participants with recent olfactory function loss consulting in the Lariboisière Hospital (Paris, France) in the context of the COVID-19 screening care for a suspected or confirmed SARS-CoV-2 infection were included during spring and summer of 2020. We also recruited participants with long-lasting/recurrent loss of smell after onset of acute COVID-19 symptoms. Those patients were recruited at the Hotel Dieu Hospital clinic dedicated for patients with long COVID-19. Among these patients, we included a control patient without loss of smell, consulting for long-term dysgeusia, vertigo, paresthesia, and evocative of COVID-19–associated neuroinvasion. Acute illness for those patients was always symptomatic and was either certain if virologically documented [at least one positive SARS-CoV-2 RT-PCR result or positive SARS-CoV-2 serology with immunoglobulin G (IgG) and/or IgM antibodies] or probable if at least one major criterion: anosmia/ageusia, contact with a PCR-conformed case, typical bilateral pneumonia on computed tomography scan, or three minor criteria among fever, headaches, fatigue, myalgias, cough, chest pain, chest tightness, unexplained tachycardia, diarrhea, and chilblains. We also recruited in this study control participants consulting in the ENT Department at the Lariboisière Hospital (Paris, France) with no biologically confirmed COVID-19 or suspected COVID-19 in the past 8 weeks and no symptoms suggestive of COVID-19 or another respiratory disease and therefore no recent taste and smell function loss.

All the research participants were included at the Lariboisière Hospital, Paris. They received an oral and written information about the research. Informed consent was obtained by the investigator before any intervention related to the research. The CovidSmell study was performed according to the approved protocol. All patients had a detailed standardized clinical and rhinological examination performed by a certified ENT physician. The following measures were performed at inclusion: (i) taste and olfactory function evaluation by a self-questionnaire taste and smell survey (*48*) and a visual analog scale (VAS) (*49*), and (ii) nasal brushing for collection of neuroepithelium cells and olfactory mucus. The participants self-assessed their smell and taste perception using a 100-mm VAS, where 0 mm indicated the inability to smell or taste and 100 mm indicated normal smell or taste perception (*49*).

Human nasal cytobrush sampling

A certified ENT physician sampled the olfactory mucosa of each participant by nasal brushing with safety precautions and after local xylocaine application (lidocaine, 5%) following the method previously described (*30*). Briefly, sampling was performed with a sterile 3.5-mm endocervical brush (02.104, Gyneas, Goussainville, France) inserted and gently rolled five times around the inside of both nostrils (360°). Swabs (one per nostril) were placed on ice immediately after collection and frozen at −80°C or put in formalin solution 10% neutral-buffered (HT-5011-1CS, Sigma-Aldrich).

Production and titration of SARS-CoV-2 virus

The strain 2019-nCoV/IDF0372/2020 [European Virus Archive (EVA-GLOBAL) collection, Ref-SKU: 014V-03890] was provided by S. Van der Werf, Institut Pasteur, Paris. Viral stocks were produced on Vero-E6 cells infected at a multiplicity of infection of 1×10^{-4} PFU. The virus was harvested 3 days after infection, clarified, and then aliquoted before storage at −80°C. Viral stocks were titrated on Vero-E6 cells by classical plaque assay using semisolid overlays (Avicel, RC581-NFDR080I, DuPont) (*50*).

SARS-CoV-2 model in hamsters

Male and female Syrian hamsters (*M. auratus*) of 5 to 6 weeks of age (average weight of 60 to 80 g) were purchased from Janvier Laboratories and handled under specific pathogen–free conditions. Hamsters were housed by groups of four animals in isolators in a biosafety level 3 facility, with ad libitum access to water and food. Before any manipulation, animals underwent an acclimation period of 1 week. Animal infection was performed as previously described with few modifications (*23*). Briefly, the animals were anesthetized with an intraperitoneal injection of ketamine (200 mg/kg; Imalgène 1000, Merial) and xylazine (10 mg/kg; Rompun, Bayer), and 100 µl of physiological solution containing 6×10^4 PFU of SARS-CoV-2 (strain 2019-nCoV/IDF0372/2020, from S. van der Werf) was administered intranasally to each animal (50 µl per nostril). Mock-infected animals received the physiological solution only. Infected and mock-infected animals were housed in separated isolators, and all hamsters were followed up daily when the body weight and the clinical score were noted. The clinical score was based on a cumulative 0 to 4 scale: ruffled fur, slow movements, apathy, and stress when manipulated. At predefined time points after infection, animals were submitted to behavioral tests or euthanized, when samples of nasal turbinates, trachea, lungs, and the brain (separated in olfactory bulbs, cerebellum, cortex, and brain stem) were collected, immediately frozen at −80°C, or formalin-fixed after transcardial perfusion with a physiological solution containing heparin (5×10^3 U/ml) (Choay, Sanofi) followed by 4% neutral-buffered formaldehyde.

Behavioral tests

All behavioral assessment was performed in isolators in a biosafety level 3 facility that we specially equipped for that.

Sucrose preference test

We measured taste in hamsters by a sucrose preference test based on a two-bottle choice paradigm that paired 2% sucrose with regular water (*51*). A reduction in the sucrose preference ratio in experimental infected relative to mock animal is indicative of taste abnormalities. After 6 hours of water deprivation, we conducted an individual overnight testing that corresponds to a natural activity period of the hamster. The preference was calculated using the following formula:

preference = sucrose intake/total intake × 100%. The total intake value is the sum of the sucrose intake value and the regular water intake.

Buried food finding test

To assess olfaction, we used the buried food finding test as previously described (*52*) with few modifications. Hamsters were used only once for each test. Four days before testing, hamsters received chocolate cereals (Coco Pops, Kellogg's) that they ate within 1 hour. Twenty hours before testing, hamsters were fasted and then individually placed into a fresh cage (37 cm by 29 cm by 18 cm) with clean standard bedding for 20 min. Hamsters were placed in another similar cage for 2 min when about 10 to 12 pieces of cereals were hidden in 1.5-cm bedding in a corner of the test cage. The tested hamster was then placed in the opposite corner, and the latency to find the food (defined as the time to locate cereals and start digging) was recorded using a chronometer. The test was carried out during a 15-min period. As soon as food was uncovered, hamsters were removed from the cage. One minute later, hamsters performed the same test but with visible chocolate cereals, positioned upon the bedding.

Scanning electron microscopy

For scanning electron microscopy, after animal transcardial perfusion in phosphate-buffered saline (PBS) and then 4% neutral-buffered formaldehyde, hamster whole heads and lungs were fixed in formalin solution 10% neutral-buffered (HT-5011-1CS, Sigma-Aldrich), for 1 week at 4°C to allow neutralization of the virus. Lung and olfactory epithelium small samples were then finely dissected and postfixed by incubation in 2.5% glutaraldehyde in 0.1 M cacodylate buffer for 1 hour at room temperature and then 12 hours at 4°C. The samples were washed in 0.1 M cacodylate and then several times in water and processed by alternating incubations in 1% osmium tetroxide and 0.1 M thiocarbohydrazide (OTOTO method), as previously described (*53*). After dehydration by incubation in increasing concentrations of ethanol, samples were critical point dried, mounted on a stub, and analyzed by field-emission scanning electron microscopy with a Jeol JSM6700F operating at 3 kV.

Immunofluorescence

Tissues from paraformaldehyde (PFA)–perfused animals were postfixed 1 week in 4% PFA, and olfactory brushes from patients were kept in PFA until further use. After postfixation, hamster whole heads (without skin and lower jaw) were decalcified in TBD-2 (6764003, Thermo Fisher Scientific) for 3 to 5 days and then sagitally cut in half and rinsed in PBS. Organs or brushes were then washed in PBS and dehydrated in 30% sucrose. They were then embedded in optimal cutting temperature (O.C.T.) compound (4583, Tissue-Tek), frozen on dry ice, and cryostat-sectioned into 20-µm-thick (hamster organs) or 14-µm-thick (brushes) sections. Sections were rinsed in PBS, and epitope retrieval was performed by incubating sections for 20 min in citrate buffer (pH 6.0; C-9999, Sigma-Aldrich) at 96°C for 20 min, or overnight at 60°C for whole head sections because they are prone to detaching from the slides. Sections were then blocked in PBS supplemented with 10% goat serum, 4% fetal calf serum, and 0.4% Triton X-100 for 2 hours at room temperature, followed by overnight incubation at 4°C with primary antibodies: rat anti-CD11b (1/100; 550282, BD Biosciences), rabbit anti-SARS-CoV NP (1/500; provided by N. Escriou, Institut Pasteur, Paris), mouse anti-OMP (1/250; sc-365818, Santa Cruz Biotechnology), chicken anti-Iba1 (1/500; 234006, Synaptic Systems), mouse anti-Tuj1 (1/250; MA1-118, Thermo Fisher Scientific), mouse anti-PGP9.5 (1/500; ab8189, Abcam), and rabbit anti-cleaved caspase-3 (1/250; Cell Signaling Technology, Asp^{175}). After rinsing, slides were incubated with the appropriate secondary antibodies (1/500; goat anti-rat Alexa Fluor 546, A11081; goat anti-rabbit Alexa Fluor 488, A11034; goat anti-mouse IgG2a Alexa Fluor 546, A21133; goat anti-chicken Alexa Fluor 647, A32933; Invitrogen) for 2 hours at room temperature. All sections were then counterstained with Hoechst (H3570, Invitrogen), rinsed thoroughly in PBS, and mounted in Fluoromount-G (15586276, Invitrogen) before observation with a Zeiss LM 710 inverted confocal microscope. Quantification of cells was performed using ImageJ in a semiautomated manner.

RNA isolation and transcriptional analyses by qPCR from human nasal cytobrushes

Frozen cytobrush samples were incubated with TRIzol (15596026, Invitrogen) during 5 min, and the total RNA was extracted using the Direct-zol RNA MicroPrep Kit (R2062, Zymo Research). The presence of the SARS-CoV-2 in these samples was evaluated by one-step qRT-PCR in a final volume of 25 µl per reaction in 96-well PCR plates using a thermocycler (7500 Real-Time PCR System, Applied Biosystems). Briefly, 5 µl of diluted RNA (1:10) was added to 20 µl of SuperScript III Platinum One-Step qRT-PCR mix (Invitrogen 11746-100) containing 12.5 µl of reaction mix, 0.4 µl of 50 mM $MgSO_4$, 1.0 µl of SuperScript RT, and 6.1 µl of nuclease-free water containing the nCoV_IP2 primers targeting the RdRp gene (nCoV_IP2-12669 forward: 5′-ATGAGCTTAGTCCTGTTG-3′; nCoV_IP2-12759 reverse: 5′-CTCCCTTTGTTGTGTTGT-3′) at a final concentration of 1 µM (*54*). The amplification conditions were as follows: 1 cycle of 55°C for 20 min, 1 cycle of 95°C for 3 min, 50 cycles of 95°C for 15 s and 58°C for 30 s, and 1 cycle of 40°C for 30 s, followed by a melt curve, from 60° to 95°C. The viral load quantification in these samples was assessed using a TaqMan one-step qRT-PCR (Invitrogen 11732-020), with the same nCoV_IP2 primers and the nCoV_IP2 probe (5′-FAM-AGATGTCTTGTGCTGCCGGTA-3′-TAMRA) at a final concentration of 1 µM (*54*).

The detection of genomic and subgenomic SARS-CoV-2 RNA was based on the E gene (*54*) using a TaqMan one-step qRT-PCR (Invitrogen 11732-020): To detect the genomic RNA, we used the E_sarbeco primers and probe (E_Sarbeco_F1 5′-ACAGGTACGTTAATAGTTAATAGCGT-3′; E_Sarbeco_R2 5′-ATATTGCAGCAGTACGCACACA-3′; E_Sarbeco_Probe FAM-5′-ACACTAGCCATCCTTACTGCGCTTCG-3′-TAMRA). The detection of subgenomic SARS-CoV-2 RNA was achieved by replacing the E_Sarbeco_F1 primer by the CoV2sgLead primer (CoV2sgLead forward: 5′-CGATCTCTTGTAGATCTGTTCTC-3′). A synthetic gene encoding the PCR target sequences was ordered from Thermo Fisher Scientific. A PCR product was amplified using Phusion High-Fidelity DNA Polymerase (Thermo Fisher Scientific) and in vitro transcribed by means of RiboMAX T7 kit (Promega). RNA was quantified using Qubit RNA HS Assay kit (Thermo Fisher Scientific), normalized, and used as a positive control to quantify RNA absolute copy number.

Total RNA from human cytobrushes was also reverse-transcribed to first-strand complementary DNA (cDNA) using the SuperScript IV VILO Master Mix (11766050, Invitrogen). To quantify host inflammatory mediators' transcripts (IL-6, CXCL10, CCL5, Mx1, and ISG20), qPCR was performed in a final volume of 10 µl per reaction in 384-well PCR plates using a thermocycler (QuantStudio 6 Flex, Applied Biosystems). Briefly, 2.5 µl of cDNA (12.5 ng) was added to 7.5 µl of a master mix containing 5 µl of Power SYBR green mix

(4367659, Applied Biosystems) and 2.5 μl of nuclease-free water containing predesigned primers (no. 249900, Qiagen; QuantiTect Primer Assays *IL-6*: QT00083720; *CXCL10*: QT01003065; CCL5: QT00090083; *Mx1*: QT00090895; *ISG20*: QT00225372; *OMP*: QT00237055; and *GAPDH*: QT00079247). The amplification conditions were as follows: 95°C for 10 min, 45 cycles of 95°C for 15 s, and 60°C for 1 min, followed by a melt curve, from 60° to 95°C. Variations in the gene expression were calculated as the *n*-fold change in expression in the tissues compared with the tissues of the control #1.

RNA isolation and transcriptional analyses by qPCR from golden hamsters' tissues

Frozen tissues were homogenized with TRIzol (15596026, Invitrogen) in Lysing Matrix D 2-ml tubes (116913100, MP Biomedicals) using the FastPrep-24 system (MP Biomedicals) and the following scheme: homogenization at 6.5 m/s during 60 s and centrifugation at 12,000*g* during 2 min at 4°C. The supernatants were collected, and the total RNA was then extracted using the Direct-zol RNA MicroPrep Kit (R2062, Zymo Research: olfactory bulb, trachea, and nasal turbinates) or MiniPrep Kit (R2052, Zymo Research: lung, brain stem, cerebral cortex, and cerebellum) and reverse-transcribed to first-strand cDNA using the using the SuperScript IV VILO Master Mix (11766050, Invitrogen). qPCR was performed in a final volume of 10 μl per reaction in 384-well PCR plates using a thermocycler (QuantStudio 6 Flex, Applied Biosystems). Briefly, 2.5 μl of cDNA (12.5 ng) was added to 7.5 μl of a master mix containing 5 μl of Power SYBR green mix (4367659, Applied Biosystems) and 2.5 μl of nuclease-free water with the nCoV_IP2 primers (nCoV_IP2-12669 forward: 5′-ATGAGCTTAGTCCTGTTG-3′; nCoV_IP2-12759 reverse: 5′-CTCCCTTTGTTGTGTTGT-3′) at a final concentration of 1 μM. The amplification conditions were as follows: 95°C for 10 min, 45 cycles of 95°C for 15 s, and 60°C for 1 min, followed by a melt curve, from 60° to 95°C. Viral load quantification in hamster tissues was assessed by linear regression using a standard curve of eight known quantities of plasmids containing the *RdRp* sequence (ranging from 10^7 to 10^0 copies). The threshold of detection was established as 200 viral copies/μg of RNA. The golden hamsters' gene targets were selected for quantifying host inflammatory mediators' transcripts in the tissues using the *Hprt* (hypoxanthine phosphoribosyltransferase) and the γ-*actin* genes as reference (table S6). Variations in the gene expression were calculated as the *n*-fold change in expression in the tissues from the infected hamsters compared with the tissues of the uninfected ones using the $2^{-\Delta\Delta Ct}$ method (*55*).

Viral titration in human nasal cytobrushes and in golden hamsters' brains

Frozen cytobrushes samples of the patients #14 and #15 and the controls #3 and #4 were incubated with 1 ml of ice-cold Dulbecco's modified Eagle's medium (DMEM) supplemented with 1% penicillin/streptomycin (15140148, Thermo Fisher Scientific) during 5 min. Frozen fragments of hamster tissues (lung, olfactory bulb, brain stem, cerebral cortex, and cerebellum) were weighted and homogenized with 1 ml of ice-cold DMEM supplemented with 1% penicillin/streptomycin in Lysing Matrix M 2-ml tubes (116923050-CF, MP Biomedicals) using the FastPrep-24 system (MP Biomedicals) and the following scheme: homogenization at 4.0 m/s during 20 s, incubation at 4°C during 2 min, and new homogenization at 4.0 m/s during 20 s. The tubes were centrifuged at 10,000*g* during 1 min at 4°C. The supernatants were titrated on Vero-E6 cells by classical plaque assays using semisolid overlays (Avicel, RC581-NFDR080I, DuPont) (*50*). RNA was isolated from the supernatants using TRIzol LS (10296028, Invitrogen) and the Direct-zol RNA MicroPrep Kit (R2062, Zymo Research) as described above.

Transcriptomics analysis in golden hamsters' olfactory bulb

RNA preparation was used to construct strand-specific single-end cDNA libraries according to the manufacturers' instructions (TruSeq Stranded mRNA sample prep kit, Illumina). Illumina NextSeq 500 sequencer was used to sequence libraries. The complete RNA-seq analysis approach is described in the Supplementary Materials.

Statistical analysis

Statistical analysis was performed using Stata 16 (StataCorp LLC, Texas, USA) and Prism software (GraphPad, version 8, San Diego, USA), with $P < 0.05$ considered significant. Quantitative data were compared across groups using Mann-Whitney nonparametric test. Categorical data were compared between groups using Fisher's exact test. Associations between the viral load, the olfactory and taste scores, the expression of cytokines, and the time from the first disease symptom were estimated with Spearman nonparametric test. In the animal experiences, time to event was analyzed using Kaplan-Meier estimates and compared across groups using the log-rank test. The degree of marker expression at different dpi was compared to the expression before infection using Kruskal-Wallis followed by the Dunn's multiple comparison test for unmatched data.

SUPPLEMENTARY MATERIALS

stm.sciencemag.org/cgi/content/full/13/596/eabf8396/DC1
Materials and Methods
Figs. S1 to S5
Tables S1 to S6
Data files S1 and S2
References

View/request a protocol for this paper from *Bio-protocol*.

REFERENCES AND NOTES

1. WHO, WHO Coronavirus Disease (COVID-19) Dashboard (2020); https://covid19.who.int/.
2. J. Helms, S. Kremer, H. Merdji, R. Clere-Jehl, M. Schenck, C. Kummerlen, O. Collange, C. Boulay, S. Fafi-Kremer, M. Ohana, M. Anheim, F. Meziani, Neurologic features in severe SARS-CoV-2 infection. *N. Engl. J. Med.* **382**, 2268–2270 (2020).
3. C. Qiu, C. Cui, C. Hautefort, A. Haehner, J. Zhao, Q. Yao, H. Zeng, E. J. Nisenbaum, L. Liu, Y. Zhao, D. Zhang, C. G. Levine, I. Cejas, Q. Dai, M. Zeng, P. Herman, C. Jourdaine, K. de With, J. Draf, B. Chen, D. T. Jayaweera, J. C. Denneny III, R. Casiano, H. Yu, A. A. Eshraghi, T. Hummel, X. Liu, Y. Shu, H. Lu, Olfactory and gustatory dysfunction as an early identifier of COVID-19 in adults and children: An international multicenter study. *Otolaryngol. Head Neck Surg.* **163**, 714–721 (2020).
4. M. S. Xydakis, P. Dehgani-Mobaraki, E. H. Holbrook, U. W. Geisthoff, C. Bauer, C. Hautefort, P. Herman, G. T. Manley, D. M. Lyon, C. Hopkins, Smell and taste dysfunction in patients with COVID-19. *Lancet Infect. Dis.* **20**, 1015–1016 (2020).
5. L. Cantuti-Castelvetri, R. Ojha, L. D. Pedro, M. Djannatian, J. Franz, S. Kuivanen, F. van der Meer, K. Kallio, T. Kaya, M. Anastasina, T. Smura, L. Levanov, L. Szirovicza, A. Tobi, H. Kallio-Kokko, P. Österlund, M. Joensuu, F. A. Meunier, S. J. Butcher, M. S. Winkler, B. Mollenhauer, A. Helenius, O. Gokce, T. Teesalu, J. Hepojoki, O. Vapalahti, C. Stadelmann, G. Balistreri, M. Simons, Neuropilin-1 facilitates SARS-CoV-2 cell entry and infectivity. *Science* **370**, 856–860 (2020).
6. T. Moriguchi, N. Harii, J. Goto, D. Harada, H. Sugawara, J. Takamino, M. Ueno, H. Sakata, K. Kondo, N. Myose, A. Nakao, M. Takeda, H. Haro, O. Inoue, K. Suzuki-Inoue, K. Kubokawa, S. Ogihara, T. Sasaki, H. Kinouchi, H. Kojin, M. Ito, H. Onishi, T. Shimizu, Y. Sasaki, N. Enomoto, H. Ishihara, S. Furuya, T. Yamamoto, S. Shimada, A first case of meningitis/encephalitis associated with SARS-Coronavirus-2. *Int. J. Infect. Dis.* **94**, 55–58 (2020).
7. M. Hoffmann, H. Kleine-Weber, S. Schroeder, N. Krüger, T. Herrler, S. Erichsen, T. S. Schiergens, G. Herrler, N.-H. Wu, A. Nitsche, M. A. Müller, C. Drosten, S. Pöhlmann, SARS-CoV-2 cell entry depends on ACE2 and TMPRSS2 and is blocked by a clinically proven protease inhibitor. *Cell* **181**, 271–280.e8 (2020).

8. Y. J. Hou, K. Okuda, C. E. Edwards, D. R. Martinez, T. Asakura, K. H. Dinnon III, T. Kato, R. E. Lee, B. L. Yount, T. M. Mascenik, G. Chen, K. N. Olivier, A. Ghio, L. V. Tse, S. R. Leist, L. E. Gralinski, A. Schäfer, H. Dang, R. Gilmore, S. Nakano, L. Sun, M. L. Fulcher, A. Livraghi-Butrico, N. I. Nicely, M. Cameron, C. Cameron, D. J. Kelvin, A. de Silva, D. M. Margolis, A. Markmann, L. Bartelt, R. Zumwalt, F. J. Martinez, S. P. Salvatore, A. Borczuk, P. R. Tata, V. Sontake, A. Kimple, I. Jaspers, W. K. O'Neal, S. H. Randell, R. C. Boucher, R. S. Baric, SARS-CoV-2 reverse genetics reveals a variable infection gradient in the respiratory tract. *Cell* **182**, 429–446.e14 (2020).
9. A. Y. Han, L. Mukdad, J. L. Long, I. A. Lopez, Anosmia in COVID-19: Mechanisms and significance. *Chem. Senses* **45**, 423–428 (2020).
10. D. M. Durrant, S. Ghosh, R. S. Klein, The olfactory bulb: An immunosensory effector organ during neurotropic viral infections. *ACS Chem. Neurosci.* **7**, 464–469 (2016).
11. A. Ramani, L. Müller, P. N. Ostermann, E. Gabriel, P. Abida-Islam, A. Müller-Schiffmann, A. Mariappan, O. Goureau, H. Gruell, A. Walker, M. Andrée, S. Hauka, T. Houwaart, A. Dilthey, K. Wohlgemuth, H. Omran, F. Klein, D. Wieczorek, O. Adams, J. Timm, C. Korth, H. Schaal, J. Gopalakrishnan, SARS-CoV-2 targets neurons of 3D human brain organoids. *EMBO J.* **39**, e106230 (2020).
12. J. Matschke, M. Lütgehetmann, C. Hagel, J. P. Sperhake, A. S. Schröder, C. Edler, H. Mushumba, A. Fitzek, L. Allweiss, M. Dandri, M. Dottermusch, A. Heinemann, S. Pfefferle, M. Schwabenland, D. Sumner Magruder, S. Bonn, M. Prinz, C. Gerloff, K. Püschel, S. Krasemann, M. Aepfelbacher, M. Glatzel, Neuropathology of patients with COVID-19 in Germany: A post-mortem case series. *Lancet Neurol.* **19**, 919–929 (2020).
13. V. G. Puelles, M. Lütgehetmann, M. T. Lindenmeyer, J. P. Sperhake, M. N. Wong, L. Allweiss, S. Chilla, A. Heinemann, N. Wanner, S. Liu, F. Braun, S. Lu, S. Pfefferle, A. S. Schröder, C. Edler, O. Gross, M. Glatzel, D. Wichmann, T. Wiech, S. Kluge, K. Pueschel, M. Aepfelbacher, T. B. Huber, Multiorgan and renal tropism of SARS-CoV-2. *N. Engl. J. Med.* **383**, 590–592 (2020).
14. M. Eliezer, A.-L. Hamel, E. Houdart, P. Herman, J. Housset, C. Jourdaine, C. Eloit, B. Verillaud, C. Hautefort, Loss of smell in patients with COVID-19: MRI data reveal a transient edema of the olfactory clefts. *Neurology* **95**, e3145–e3152 (2020).
15. S. Saussez, J. R. Lechien, C. Hopkins, Anosmia: An evolution of our understanding of its importance in COVID-19 and what questions remain to be answered. *Eur. Arch. Otorhinolaryngol.* , 1–5 (2020).
16. M. F. V. V. Aragão, M. C. Leal, O. Q. Cartaxo Filho, T. M. Fonseca, M. M. Valença, Anosmia in COVID-19 associated with injury to the olfactory bulbs evident on MRI. *Am. J. Neuroradiol.* **41**, 1703–1706 (2020).
17. T. Laurendon, T. Radulesco, J. Mugnier, M. Gérault, C. Chagnaud, A.-A. El Ahmadi, A. Varoquaux, Bilateral transient olfactory bulb edema during COVID-19–related anosmia. *Neurology* **95**, 224–225 (2020).
18. J. Luan, Y. Lu, X. Jin, L. Zhang, Spike protein recognition of mammalian ACE2 predicts the host range and an optimized ACE2 for SARS-CoV-2 infection. *Biochem. Biophys. Res. Commun.* **526**, 165–169 (2020).
19. P. B. McCray Jr., L. Pewe, C. Wohlford-Lenane, M. Hickey, L. Manzel, L. Shi, J. Netland, H. P. Jia, C. Halabi, C. D. Sigmund, D. K. Meyerholz, P. Kirby, D. C. Look, S. Perlman, Lethal infection of K18-*hACE2* mice infected with severe acute respiratory syndrome coronavirus. *J. Virol.* **81**, 813–821 (2006).
20. R.-D. Jiang, M.-Q. Liu, Y. Chen, C. Shan, Y.-W. Zhou, X.-R. Shen, Q. Li, L. Zhang, Y. Zhu, H.-R. Si, Q. Wang, J. Min, X. Wang, W. Zhang, B. Li, H.-J. Zhang, R. S. Baric, P. Zhou, X.-L. Yang, Z.-L. Shi, Pathogenesis of SARS-CoV-2 in transgenic mice expressing human angiotensin-converting enzyme 2. *Cell* **182**, 50–58.e8 (2020).
21. S.-H. Sun, Q. Chen, H.-J. Gu, G. Yang, Y.-X. Wang, X.-Y. Huang, S.-S. Liu, N.-N. Zhang, X.-F. Li, R. Xiong, Y. Guo, Y.-Q. Deng, W.-J. Huang, Q. Liu, Q.-M. Liu, Y.-L. Shen, Y. Zhou, X. Yang, T.-Y. Zhao, C.-F. Fan, Y.-S. Zhou, C.-F. Qin, Y.-C. Wang, A mouse model of SARS-CoV-2 infection and pathogenesis. *Cell Host Microbe* **28**, 124–133.e4 (2020).
22. E. S. Winkler, A. L. Bailey, N. M. Kafai, S. Nair, B. T. McCune, J. Yu, J. M. Fox, R. E. Chen, J. T. Earnest, S. P. Keeler, J. H. Ritter, L.-I. Kang, S. Dort, A. Robichaud, R. Head, M. J. Holtzman, M. S. Diamond, SARS-CoV-2 infection of human ACE2-transgenic mice causes severe lung inflammation and impaired function. *Nat. Immunol.* **21**, 1327–1335 (2020).
23. J. F.-W. Chan, A. J. Zhang, S. Yuan, V. K.-M. Poon, C. C.-S. Chan, A. C.-Y. Lee, W.-M. Chan, Z. Fan, H.-W. Tsoi, L. Wen, R. Liang, J. Cao, Y. Chen, K. Tang, C. Luo, J.-P. Cai, K.-H. Kok, H. Chu, K.-H. Chan, S. Sridhar, Z. Chen, H. Chen, K. K.-W. To, K.-Y. Yuen, Simulation of the clinical and pathological manifestations of coronavirus disease 2019 (COVID-19) in a golden Syrian hamster model: Implications for disease pathogenesis and transmissibility. *Clin. Infect. Dis.* **71**, 2428–2446 (2020).
24. S. F. Sia, L.-M. Yan, A. W. H. Chin, K. Fung, K.-T. Choy, A. Y. L. Wong, P. Kaewpreedee, R. A. P. M. Perera, L. L. M. Poon, J. M. Nicholls, M. Peiris, H.-L. Yen, Pathogenesis and transmission of SARS-CoV-2 in golden hamsters. *Nature* **583**, 834–838 (2020).
25. M. Imai, K. Iwatsuki-Horimoto, M. Hatta, S. Loeber, P. J. Halfmann, N. Nakajima, T. Watanabe, M. Ujie, K. Takahashi, M. Ito, S. Yamada, S. Fan, S. Chiba, M. Kuroda, L. Guan, K. Takada, T. Armbrust, A. Balogh, Y. Furusawa, M. Okuda, H. Ueki, A. Yasuhara, Y. Sakai-Tagawa, T. J. S. Lopes, M. Kiso, S. Yamayoshi, N. Kinoshita, N. Ohmagari, S.-i. Hattori, M. Takeda, H. Mitsuya, F. Krammer, T. Suzuki, Y. Kawaoka, Syrian hamsters as a small animal model for SARS-CoV-2 infection and countermeasure development. *Proc. Natl. Acad. Sci. U.S.A.* **117**, 16587–16595 (2020).
26. A. J. Zhang, A. C.-Y. Lee, H. Chu, J. F.-W. Chan, Z. Fan, C. Li, F. Liu, Y. Chen, S. Yuan, V. K.-M. Poon, C. C.-S. Chan, J.-P. Cai, K. L.-K. Wu, S. Sridhar, Y.-S. Chan, K.-Y. Yuen, Severe acute respiratory syndrome coronavirus 2 infects and damages the mature and immature olfactory sensory neurons of hamsters. *Clin. Infect. Dis.* , ciaa995 (2020).
27. B. Bryche, A. St Albin, S. Murri, S. Lacôte, C. Pulido, M. Ar Gouilh, S. Lesellier, A. Servat, M. Wasniewski, E. Picard-Meyer, E. Monchatre-Leroy, R. Volmer, O. Rampin, R. Le Goffic, P. Marianneau, N. Meunier, Massive transient damage of the olfactory epithelium associated with infection of sustentacular cells by SARS-CoV-2 in golden Syrian hamsters. *Brain Behav. Immun.* **89**, 579–586 (2020).
28. S. E. Arnold, E. B. Lee, P. J. Moberg, L. Stutzbach, H. Kazi, L.-Y. Han, V. M. Y. Lee, J. Q. Trojanowski, Olfactory epithelium amyloid-β and paired helical filament-tau pathology in Alzheimer disease. *Ann. Neurol.* **67**, 462–469 (2010).
29. C. D. Orrú, M. Bongianni, G. Tonoli, S. Ferrari, A. G. Hughson, B. R. Groveman, M. Fiorini, M. Pocchiari, S. Monaco, B. Caughey, G. Zanusso, A test for Creutzfeldt-Jakob disease using nasal brushings. *N. Engl. J. Med.* **371**, 519–529 (2014).
30. L. Bertero, S. B. Joseph, M. Trunfio, T. Allice, S. Catera, D. Imperiale, P. Cassoni, L. P. Kincer, V. Pirriatore, V. Ghisetti, E. Amasio, G. Zanusso, S. Bonora, G. Di Perri, A. Calcagno, HIV-1 detection in the olfactory mucosa of HIV-1-infected participants. *AIDS* **33**, 665–674 (2019).
31. M. Gousseff, P. Penot, L. Gallay, D. Batisse, N. Benech, K. Bouiller, R. Collarino, A. Conrad, D. Slama, C. Joseph, A. Lemaignen, F.-X. Lescure, B. Levy, M. Mahevas, B. Pozzetto, N. Vignier, B. Wyplosz, D. Salmon, F. Goehringer, E. Botelho-Nevers; COCOREC Study Group, Clinical recurrences of COVID-19 symptoms after recovery: Viral relapse, reinfection or inflammatory rebound? *J. Infect.* **81**, 816–846 (2020).
32. C. M. Chiesa-Estomba, J. R. Lechien, T. Radulesco, J. Michel, L. J. Sowerby, C. Hopkins, S. Saussez, Patterns of smell recovery in 751 patients affected by the COVID-19 outbreak. *Eur. J. Neurol.* **27**, 2318–2321 (2020).
33. R. Wölfel, V. M. Corman, W. Guggemos, M. Seilmaier, S. Zange, M. A. Müller, D. Niemeyer, T. C. Jones, P. Vollmar, C. Rothe, M. Hoelscher, T. Bleicker, S. Brünink, J. Schneider, R. Ehmann, K. Zwirglmaier, C. Drosten, C. Wendtner, Virological assessment of hospitalized patients with COVID-2019. *Nature* **581**, 465–469 (2020).
34. A. Carmo, J. Pereira-Vaz, V. Mota, A. Mendes, C. Morais, A. C. da Silva, E. Camilo, C. S. Pinto, E. Cunha, J. Pereira, M. Coucelo, P. Martinho, L. Correia, G. Marques, L. Araújo, F. Rodrigues, Clearance and persistence of SARS-CoV-2 RNA in patients with COVID-19. *J. Med. Virol.* **92**, 2227–2231 (2020).
35. S. Ikegami, R. Benirschke, T. Flanagan, N. Tanna, T. Klein, R. Elue, P. Debosz, J. Mallek, G. Wright, P. Guariglia, J. Kang, T. J. Gniadek, Persistence of SARS-CoV-2 nasopharyngeal swab PCR positivity in COVID-19 convalescent plasma donors. *Transfusion* **60**, 2962–2968 (2020).
36. A. Carfì, R. Bernabei, F. Landi; Gemelli Against COVID-19 Post-Acute Care Study Group, Persistent symptoms in patients after acute COVID-19. *JAMA* **324**, 603–605 (2020).
37. L. K. Vibholm, S. S. F. Nielsen, M. H. Pahus, G. S. Frattari, R. Olesen, R. Andersen, I. Monrad, A. H. F. Andersen, M. M. Thomsen, C. V. Konrad, S. D. Andersen, J. F. Højen, J. D. Gunst, L. Østergaard, O. S. Søgaard, M. H. Schleimann, M. Tolstrup, SARS-CoV-2 persistence is associated with antigen-specific CD8 T-cell responses. *EBioMedicine* **64**, 103230 (2021).
38. C. Gaebler, Z. Wang, J. C. C. Lorenzi, F. Muecksch, S. Finkin, M. Tokuyama, A. Cho, M. Jankovic, D. Schaefer-Babajew, T. Y. Oliveira, M. Cipolla, C. Viant, C. O. Barnes, Y. Bram, G. Breton, T. Hägglöf, P. Mendoza, A. Hurley, M. Turroja, K. Gordon, K. G. Millard, V. Ramos, F. Schmidt, Y. Weisblum, D. Jha, M. Tankelevich, G. Martinez-Delgado, J. Yee, R. Patel, J. Dizon, C. Unson-O'Brien, I. Shimeliovich, D. F. Robbiani, Z. Zhao, A. Gazumyan, R. E. Schwartz, T. Hatziioannou, P. J. Bjorkman, S. Mehandru, P. D. Bieniasz, M. Caskey, M. C. Nussenzweig, Evolution of antibody immunity to SARS-CoV-2. *Nature* **591**, 639–644 (2021).
39. J. Meinhardt, J. Radke, C. Dittmayer, J. Franz, C. Thomas, R. Mothes, M. Laue, J. Schneider, S. Brünink, S. Greuel, M. Lehmann, O. Hassan, T. Aschman, E. Schumann, R. L. Chua, C. Conrad, R. Eils, W. Stenzel, M. Windgassen, L. Rößler, H.-H. Goebel, H. R. Gelderblom, H. Martin, A. Nitsche, W. J. Schulz-Schaeffer, S. Hakroush, M. S. Winkler, B. Tampe, F. Scheibe, P. Körtvélyessy, D. Reinhold, B. Siegmund, A. A. Kühl, S. Elezkurtaj, D. Horst, L. Oesterhelweg, M. Tsokos, B. Ingold-Heppner, C. Stadelmann, C. Drosten, V. M. Corman, H. Radbruch, F. L. Heppner, Olfactory transmucosal SARS-CoV-2 invasion as port of central nervous system entry in individuals with COVID-19. *Nat. Neurosci.* **24**, 168–175 (2021).
40. K. W. Cooper, D. H. Brann, M. C. Farruggia, S. Bhutani, R. Pellegrino, T. Tsukahara, C. Weinreb, P. V. Joseph, E. D. Larson, V. Parma, M. W. Albers, L. A. Barlow, S. R. Datta,

A. Di Pizio, COVID-19 and the chemical senses: Supporting players take center stage. *Neuron* **107**, 219–233 (2020).
41. D. H. Brann, T. Tsukahara, C. Weinreb, M. Lipovsek, K. Van den Berge, B. Gong, R. Chance, I. C. Macaulay, H.-J. Chou, R. B. Fletcher, D. Das, K. Street, H. R. de Bezieux, Y.-G. Choi, D. Risso, S. Dudoit, E. Purdom, J. Mill, R. A. Hachem, H. Matsunami, D. W. Logan, B. J. Goldstein, M. S. Grubb, J. Ngai, S. R. Datta, Non-neuronal expression of SARS-CoV-2 entry genes in the olfactory system suggests mechanisms underlying COVID-19-associated anosmia. *Sci. Adv.* **6**, eabc5801 (2020).
42. R. Robinot, M. Hubert, G. D. de Melo, F. Lazarini, T. Bruel, N. Smith, S. Levallois, F. Larrous, J. Fernandes, S. Gellenoncourt, S. Rigaud, O. Gorgette, C. Thouvenot, C. Trébeau, A. Mallet, G. Duménil, S. Gobaa, R. Etournay, P.-M. Lledo, M. Lecuit, H. Bourhy, D. Duffy, V. Michel, O. Schwartz, L. A. Chakrabarti, SARS-CoV-2 infection damages airway motile cilia and impairs mucociliary clearance. *bioRxiv*, 2020.10.06.328369 (2020).
43. G. D. de Melo, F. Lazarini, F. Larrous, L. Feige, L. Kergoat, A. Marchio, P. Pineau, M. Lecuit, P.-M. Lledo, J.-P. Changeux, H. Bourhy, Anti-COVID-19 efficacy of ivermectin in the golden hamster. *bioRxiv*, 2020.11.21.392639 (2020).
44. M. Larvie, M. H. Lev, C. P. Hess, More on neurologic features in severe SARS-CoV-2 infection. *N. Engl. J. Med.* **382**, e110 (2020).
45. I. H. Solomon, E. Normandin, S. Bhattacharyya, S. S. Mukerji, K. Keller, A. S. Ali, G. Adams, J. L. Hornick, R. F. Padera Jr., P. Sabeti, Neuropathological features of Covid-19. *N. Engl. J. Med.* **383**, 989–992 (2020).
46. M. Desforges, A. Le Coupanec, P. Dubeau, A. Bourgouin, L. Lajoie, M. Dubé, P. J. Talbot, Human coronaviruses and other respiratory viruses: Underestimated opportunistic pathogens of the central nervous system? *Viruses* **12**, 14 (2019).
47. D. Yelin, E. Wirtheim, P. Vetter, A. C. Kalil, J. Bruchfeld, M. Runold, G. Guaraldi, C. Mussini, C. Gudiol, M. Pujol, A. Bandera, L. Scudeller, M. Paul, L. Kaiser, L. Leibovici, Long-term consequences of COVID-19: Research needs. *Lancet Infect. Dis.* **20**, 1115–1117 (2020).
48. N. McGettigan, P. U. Dhuibhir, M. Barrett, J. Sui, L. Balding, S. Higgins, N. O'Leary, A. Kennedy, D. Walsh, Subjective and objective assessment of taste and smell sensation in advanced cancer. *Am. J. Hosp. Palliat. Care* **36**, 688–696 (2019).
49. L. C. P. Kokubo, T. B. O. Carvalho, M. A. Fornazieri, E. M. d. C. Gomes, C. M. F. Alves, A. L. L. Sampaio, Effects of septorhinoplasty on smell perception. *Eur. Arch. Otorhinolaryngol.* **276**, 1247–1250 (2019).
50. A. Baer, K. Kehn-Hall, Viral concentration determination through plaque assays: Using traditional and novel overlay systems. *J. Vis. Exp.* , e52065 (2014).
51. J. R. Faull, B. P. Halpern, Reduction of sucrose preference in the hamster by gymnemic acid. *Physiol. Behav.* **7**, 903–907 (1971).
52. F. Lazarini, L. Katsimpardi, S. Levivien, S. Wagner, P. Gressens, N. Teissier, P.-M. Lledo, Congenital cytomegalovirus infection alters olfaction before hearing deterioration in mice. *J. Neurosci.* **38**, 10424–10437 (2018).
53. D. N. Furness, Y. Katori, B. Nirmal Kumar, C. M. Hackney, The dimensions and structural attachments of tip links in mammalian cochlear hair cells and the effects of exposure to different levels of extracellular calcium. *Neuroscience* **154**, 10–21 (2008).
54. V. M. Corman, O. Landt, M. Kaiser, R. Molenkamp, A. Meijer, D. K. Chu, T. Bleicker, S. Brünink, J. Schneider, M. L. Schmidt, D. G. Mulders, B. L. Haagmans, B. van der Veer, S. van den Brink, L. Wijsman, G. Goderski, J.-L. Romette, J. Ellis, M. Zambon, M. Peiris, H. Goossens, C. Reusken, M. P. Koopmans, C. Drosten, Detection of 2019 novel coronavirus (2019-nCoV) by real-time RT-PCR. *Euro Surveill.* **25**, 2000045 (2020).
55. M. W. Pfaffl, A new mathematical model for relative quantification in real-time RT-PCR. *Nucleic Acids Res.* **29**, e45 (2001).
56. F. de Chaumont, S. Dallongeville, N. Chenouard, N. Hervé, S. Pop, T. Provoost, V. Meas-Yedid, P. Pankajakshan, T. Lecomte, Y. Le Montagner, T. Lagache, A. Dufour, J.-C. Olivo-Marin, Icy: An open bioimage informatics platform for extended reproducible research. *Nat. Methods* **9**, 690–696 (2012).
57. S. P. Brooks, S. B. Dunnett, Tests to assess motor phenotype in mice: A user's guide. *Nat. Rev. Neurosci.* **10**, 519–529 (2009).
58. T. Cokelaer, D. Desvillechabrol, R. Legendre, M. Cardon, 'Sequana': A set of Snakemake NGS pipelines. *J. Open Source Softw.* **2**, 352 (2017).
59. J. Köster, S. Rahmann, Snakemake—A scalable bioinformatics workflow engine. *Bioinformatics* **28**, 2520–2522 (2012).
60. M. Martin, Cutadapt removes adapter sequences from high-throughput sequencing reads. *EMBnet J.* **17**, 3 (2011).
61. A. Dobin, C. A. Davis, F. Schlesinger, J. Drenkow, C. Zaleski, S. Jha, P. Batut, M. Chaisson, T. R. Gingeras, STAR: Ultrafast universal RNA-seq aligner. *Bioinformatics* **29**, 15–21 (2012).
62. Y. Liao, G. K. Smyth, W. Shi, featureCounts: An efficient general purpose program for assigning sequence reads to genomic features. *Bioinformatics* **30**, 923–930 (2014).
63. P. Ewels, M. Magnusson, S. Lundin, M. Käller, MultiQC: Summarize analysis results for multiple tools and samples in a single report. *Bioinformatics* **32**, 3047–3048 (2016).
64. M. I. Love, W. Huber, S. Anders, Moderated estimation of fold change and dispersion for RNA-seq data with DESeq2. *Genome Biol.* **15**, 550 (2014).
65. H. Varet, L. Brillet-Guéguen, J.-Y. Coppée, M.-A. Dillies, SARTools: A DESeq2- and EdgeR-based R pipeline for comprehensive differential analysis of RNA-Seq data. *PLOS ONE* **11**, e0157022 (2016).
66. H. Mi, A. Muruganujan, D. Ebert, X. Huang, P. D. Thomas, PANTHER version 14: More genomes, a new PANTHER GO-slim and improvements in enrichment analysis tools. *Nucleic Acids Res.* **47**, D419–D426 (2019).
67. R. P. Huntley, T. Sawford, P. Mutowo-Meullenet, A. Shypitsyna, C. Bonilla, M. J. Martin, C. O'Donovan, The GOA database: Gene Ontology annotation updates for 2015. *Nucleic Acids Res.* **43**, D1057–D1063 (2014).
68. E. Y. Chen, C. M. Tan, Y. Kou, Q. Duan, Z. Wang, G. V. Meirelles, N. R. Clark, A. Ma'ayan, Enrichr: Interactive and collaborative HTML5 gene list enrichment analysis tool. *BMC Bioinformatics* **14**, 128 (2013).
69. M. Kanehisa, S. Goto, KEGG: Kyoto encyclopedia of genes and genomes. *Nucleic Acids Res.* **28**, 27–30 (2000).
70. T. Cokelaer, D. Pultz, L. M. Harder, J. Serra-Musach, J. Saez-Rodriguez, BioServices: A common Python package to access biological Web Services programmatically. *Bioinformatics* **29**, 3241–3242 (2013).
71. R. P. Ribeiro-Romão, A. F. Saavedra, A. M. Da-Cruz, E. F. Pinto, O. C. Moreira, Development of real-time PCR assays for evaluation of immune response and parasite load in golden hamster (*Mesocricetus auratus*) infected by *Leishmania* (Viannia) *braziliensis*. *Parasit. Vectors* **9**, 361 (2016).
72. M. Zivcec, D. Safronetz, E. Haddock, H. Feldmann, H. Ebihara, Validation of assays to monitor immune responses in the Syrian golden hamster (*Mesocricetus auratus*). *J. Immunol. Methods* **368**, 24–35 (2011).
73. T. Schountz, C. Campbell, K. Wagner, J. Rovnak, C. Martellaro, B. L. DeBuysscher, H. Feldmann, J. Prescott, Differential innate immune responses elicited by Nipah Virus and Cedar Virus correlate with disparate in vivo pathogenesis in hamsters. *Viruses* **11**, 291 (2019).
74. B. B. Gowen, J. B. Westover, E. J. Sefing, K. W. Bailey, S. Nishiyama, L. Wandersee, D. Scharton, K.-H. Jung, T. Ikegami, MP-12 virus containing the clone 13 deletion in the NSs gene prevents lethal disease when administered after Rift Valley fever virus infection in hamsters. *Front. Microbiol.* **6**, 651 (2015).
75. R. Boudewijns, H. J. Thibaut, S. J. F. Kaptein, R. Li, V. Vergote, L. Seldeslachts, J. Van Weyenbergh, C. De Keyzer, L. Bervoets, S. Sharma, L. Liesenborghs, J. Ma, S. Jansen, D. Van Looveren, T. Vercruysse, X. Wang, D. Jochmans, E. Martens, K. Roose, D. De Vlieger, B. Schepens, T. Van Buyten, S. Jacobs, Y. Liu, J. Martí-Carreras, B. Vanmechelen, T. Wawina-Bokalanga, L. Delang, J. Rocha-Pereira, L. Coelmont, W. Chiu, P. Leyssen, E. Heylen, D. Schols, L. Wang, L. Close, J. Matthijnssens, M. Van Ranst, V. Compernolle, G. Schramm, K. Van Laere, X. Saelens, N. Callewaert, G. Opdenakker, P. Maes, B. Weynand, C. Cawthorne, G. Vande Velde, Z. Wang, J. Neyts, K. Dallmeier, STAT2 signaling restricts viral dissemination but drives severe pneumonia in SARS-CoV-2 infected hamsters. *Nat. Commun.* **11**, 5838 (2020).

Acknowledgments: We thank all participants for volunteering for the clinical study. The human sample from which strain 2019-nCoV/IDF0372/2020 was isolated has been provided by X. Lescure and Y. Yazdanpanah from the Bichat Hospital, Paris, France. We thank C. Jourdaine, Department of Otorhinolaryngology, Lariboisière Hospital, Paris, France. The clinical research ("CovidSmell") is sponsored by Institut Pasteur, Paris. We thank E. Turc and L. Lemée, Biomics Platform, C2RT, Institut Pasteur, Paris, France, supported by France Génomique (ANR-10-INBS-09-09), IBISA, and the Illumina COVID-19 Projects' offer. We also thank A. Perilhou, O. Chény, and T.-P. Bui Van, Clinical Core, CRT, Institut Pasteur, Paris, France. We thank K. Sailor, E. Poivet, G. Lepousez, and T. Sharshar for critical reading of the manuscript; S. Van der Werf (National Reference Centre for Respiratory Viruses hosted by Institut Pasteur, Paris) for the SARS-CoV-2 isolate used in this study; and N. Escriou (Innovation lab: Vaccines, Institut Pasteur, Paris) for providing the anti–SARS-CoV-2 NP antibody; and M. Berard, L. Breton, R. Chennouf, H. Diakhate, and E. Maranghi for help in implementing experiments at the Institut Pasteur animal facilities. Finally, we thank the Institut Pasteur Ultrastructural BioImaging core facility (UBI) for the access to the scanning electron microscopy equipment. **Funding:** This work was supported by the "URGENCE COVID-19" fundraising campaign of Institut Pasteur (to P.-M.L., H.B., and M.L.), the Investissements d'Avenir program managed by the Agence Nationale de la Recherche (ANR) under the reference ANR-11-IDEX-0004-02 and ANR-10-LABX-73 (to P.-M.L.), the Agence Nationale de la Recherche (ANR-15-CE37-0004-01 "SmellBrain" to P.-M.L.), the Fondation pour la Recherche Médicale (ECO201906009119 to S.L.), the Per Fumum Endowment Fund (to P.-M.L.), and the Life Insurance Company "AG2R-La Mondiale" (to P.-M.L.), the LabEx IBEID (to M.L.), Institut Pasteur core funding (to M.L.), and INSERM core funding (to M.L.). **Author contributions:** G.D.d.M., F. Lazarini, S.L., C.H., R.H., Y.M., E.R., D.S., M.L., H.B., and P.-M.L. designed research studies. F. Lazarini, G.D.d.M., S.L., F. Larrous, V.M., and L.K. performed the experiments. F. Lazarini, G.D.d.M., S.L., C.H., B.V., F. Larrous, V.M., E.K., F.D., T.C., and L.K. acquired data. F. Lazarini, G.D.d.M., S.L., F. Larrous, G.G., M.L., V.M., E.K., T.C., H.B., and P.-M.L. analyzed and discussed data. S.W. developed behavioral material for hamsters. C.H. and B.V. collected olfactory mucosa samples and acquired informed consent.

Y.M. supervised statistical analyses. F. Lazarini, G.D.d.M., and S.L. wrote the manuscript, which was edited by H.B., M.L., and P.-M.L. All authors revised and approved the final version of the manuscript. **Competing interests:** The authors declared that they have no competing interests. **Data and materials availability:** All data associated with this study are present in the paper or the Supplementary Materials. RNA-seq data are available in the European Nucleotide Archive (ENA; access number E-MTAB-10442).

Submitted 23 November 2020
Resubmitted 26 March 2021
Accepted 27 April 2021
Published First Release 3 May 2021
Published 2 June 2021
10.1126/scitranslmed.abf8396

Citation: G. D. de Melo, F. Lazarini, S. Levallois, C. Hautefort, V. Michel, F. Larrous, B. Verillaud, C. Aparicio, S. Wagner, G. Gheusi, L. Kergoat, E. Kornobis, F. Donati, T. Cokelaer, R. Hervochon, Y. Madec, E. Roze, D. Salmon, H. Bourhy, M. Lecuit, P.-M. Lledo, COVID-19–related anosmia is associated with viral persistence and inflammation in human olfactory epithelium and brain infection in hamsters. *Sci. Transl. Med.* **13**, eabf8396 (2021).

Science Translational Medicine

COVID-19–related anosmia is associated with viral persistence and inflammation in human olfactory epithelium and brain infection in hamsters

Guilherme Dias de MeloFrançoise LazariniSylvain LevalloisCharlotte HautefortVincent MichelFlorence LarrousBenjamin VerillaudCaroline AparicioSebastien WagnerGilles GheusiLauriane KergoatEtienne KornobisFlora DonatiThomas CokelaerRémi HervochonYoann MadecEmmanuel RozeDominique SalmonHervé BourhyMarc LecuitPierre-Marie Lledo

Sci. Transl. Med., 13 (596), eabf8396. • DOI: 10.1126/scitranslmed.abf8396

Sticking the nose into COVID-19

Patients with COVID-19 can develop loss of smell and/or taste. Unfortunately, the pathophysiology of these alterations remains unclear. Here, de Melo *et al.* examined the olfactory mucosa in patients with COVID-19 reporting loss of smell and detected SARS-CoV-2 viral particles and inflammation in multiple cell types in the olfactory neuroepithelium, including olfactory sensory neurons. Hamster infected with SARS-CoV-2 developed loss of smell that was associated with dissemination of the virus in the olfactory mucosa and CNS and with neuroinflammation. In four patients who developed persistent loss of smell, the authors detected lasting SARS-CoV-2 presence in the olfactory mucosa, suggesting that the prolonged relapsing anosmia in patients with COVID-19 could be due to persistent viral infection.

Science Translational Medicine (ISSN 1946-6242) is published by the American Association for the Advancement of Science. 1200 New York Avenue NW, Washington, DC 20005. The title *Science Translational Medicine* is a registered trademark of AAAS.